POLITECNICO
MILANO 1863

Politecnico di Milano

DEPARTMENT OF PHYSICS
Ph.D. Programme in Physics

Lead halide perovskite semiconductors: the role of morphological control for high performance solar cells

Supervisor
Dr. Annamaria Petrozza

Tutor
Prof. Guglielmo Lanzani

Ph.D. Candidate
Marina Gandini

«Do not undertake a project
unless it is manifestly important
and nearly impossible»
Edwin H. Land

Thesis Plan

The present work is the result of a three-years period as a Ph. D. student, under the supervision and guidance of Dr. Annamaria Petrozza. All the results included have been achieved personally in the labs of the Center for NanoScience and Technology of the Italian Insitute of Technology (IIT) in Milan, at Politecnico di Milano, unless otherwise stated. The thesis is divided into 5 chapters. Here, a brief description of the contents.

Chapter 1 A general background about the world of photovoltaics is reported. The physics of solar cells will be described shortly, to introduce the concepts that will be fundamental in the following Chapters. A review of the most recent results about hybrid and fully inorganic metal halide perovskites is described.

Chapter 2 A comprehensive description of the materials and methods employed is included. In addition, specifications about sample realization and detailed protocols for the fabrication of photovoltaic devices. A list of experimental techniques personally used during the work is comprised.

Chapter 3 The focus is on the optical properties of hybrid lead halide perovskites, aiming to highlight the strong correlation between crystalline morphology and opto-electronic behaviour of these materials. The effects of the synthesis' environmental conditions over the final morphology of perovskite self-assembled crystals will be discussed.

Chapter 4 A novel synthesis of high-quality colloidal perovskite nanocrystals is presented. Considerations about the role of many synthetic parameters will be discussed, including results obtained when these materials are embodied in a device architecture.

Appendix Last pages are dedicated to the summary of scientific publications.

Contents

Abstract

Tri-dimensional lead halide perovskite semiconductors are an emerging solution-processed class of materials that has led to great advances in the performances of solar cells since 2013, and has demonstrated good potential when embodied in light emitting devices and photodetectors. The exceptional opto-electronic properties of these materials, such as the tunable direct band-gap, the extremely high absorption coefficient, the low exciton binding energy, and the balanced ambipolar carrier transport have been extensively studied in the last few years. At the same time, many of the finer details of the device physics remain under debate. In particular, the understanding of the role of structural and chemical defects, and their effects on the properties of devices, has become imperative. Overall, the three-year work highlights the primary properties of the same class of material obtained by various synthetic routes, combining structural and morphological characterizations to the photophysical ones. The thesis work shows a direct comparison between two different approaches to the realization of a perovskite-based thin film. The first one consists in the direct crystallization of the semiconductive material onto a substrate, starting from precursors solutions, while the second one relies on the deposition of pre-formed high-quality colloidal perovskite-based nanocrystals. The first approach is the most widely used in literature. It consists in the self-organization of ionized precursors dispersed in high boiling point organic solvents, which undergo a crystallization upon thermal treatment. Chemical purity of the precursors, presence of additives, relative humidity, temperature and surface properties of the substrates employed are just few of the parameters that can deeply affect the organization of the perovskite crystalline lattice. In this case, a non-negligible level of unintentional structural and chemical defects is expected, within the bulk and at the interfaces of the crystals. Such defects can introduce localized energy levels that are confined in the band-gap of the semiconductor, creating non-radiative recombination pathways for the photo-generated charge carriers. A reproducible and reliable protocol to fabricate polycrystalline thin film, with different average-crystallite dimensions, is reported. Varying the crystallites mean size, from tens of nanometers to a few micrometers, it is possible to tune the opto-electronic behaviour of the material, directly influencing the number and the type of electrically-

active defect sites. From these results, the existence of a tight tolerance window for the optimal processing parameters of these self-assembled materials clearly emerges. A novel approach is then proposed, consisting in the realization of the solar cell active layer by the deposition of an ink composed by suspended nanoparticles. The ink formulation can be tailored prior to the film formation, meaning that the co-optimization of large-area uniform coverage with a high-quality crystal growth is no longer needed. The results obtained by following this approach are presented in the second part of the thesis. A fully inorganic cesium lead bromide ($CsPbBr_3$) perovskite has been employed in the study. Since bromide-based compounds exhibit a wide band-gap, around 2.32 eV, these materials can achieve much higher open-circuit values, extending the interest for the applications to multijunction solar cells, visible light-emitting devices and photo-electrochemical cells. A new, fast and one-step-injection synthesis is proposed, leading to the formation of stable colloidal nano-crystalline perovskite nano-particles, passivated by organic ligands. The innovative synthesis has the advantages of being a room-temperature and moisture-insensitive process, that employs only low boiling point and less toxic solvents, compared to the ones required in the standard approach. The use of ligands, composed by short alkyl chains, circumvents post-synthesis treatments typical of the longer and bulkier chains usually employed in this field. The passivating nature of the nanocrystal's ligands gives rise to extremely good photo-luminescence properties. The photo-luminescence quantum yield for the colloidal suspension is higher than 75%, and it drops to 35% after the particles have been deposited. The thin film obtained shows an amplified spontaneous emission (ASE) threshold as low as 1.5 $\mu J/cm^2$, which sets a record for not-passivated inorganic nanostructures. The optical quality observed is close to those of nanocrystals made with high-temperature hot-injection syntheses previously reported in literature. Interestingly, the quantum yield from the films prepared with bulkier ligands are comparable to the ones typically observed from the films here reported, but they remain non-conductive. Both the quantum yield and the ASE threshold values are indicative of a lower defect density compared to perovskite thin film obtained from standard direct-crystallization approaches. The $CsPbBr_3$ perovskite inks are then used to fabricate a halide perovskite nanocrystalline-based photovoltaic prototype device. The deposition of highly uniform and complete films has been uniquely facilitated by the use of low-boiling point solvents for the preparation of the colloidal suspension. Sequential deposition cycles enable a fine control over the final active-material thickness. In particular, a layer of 550 ± 50 nm, corresponding to an optical thickness of more than 1.5 OD, exhibited a power conversion efficiency of 5.4%, which is comparable to the best-performing and fully optimized devices reported so far. The solar cell exhibits short circuit current (J_{SC}) and an open circuit voltage (V_{OC}) values of 5.6 mA/cm^2 and 1.5 V, as well as a fill factor of 0.62. The value for V_{OC} is among the highest re-

ported for perovskite halides, underlying the high quality of the perovskite crystals. For a better understanding of the reference, the calculated ideal maximum V_{OC} and J_{SC} are 2.05 V and 7.78 mA/cm2 under AM1.5 illumination, considering a bandgap of about 2.38 eV. Finally, it has to be highlight that this process is fully carried out in ambient air. Moreover, the technique provides electrically stable devices. Finally, a fine analysis over the ligands' role in the device performances has been carried out. At the same time, the correlation between the nanocrystal size and the figures of merit of the devices has been investigated, highlighting the nanocrystal size-dependence of the current density in the device. The validity of this novel approach has been further demonstrated by successfully applied it to large-area deposition techniques (bar-coating), obtaining working devices with performances comparable to the previously reported ones.

Chapter 1

Introduction

Improving the quality of life while counteracting the human impact on the planet environment is one of the biggest challenges the mankind has to face right now. A realistic strategy to tackle this problem combines the reduction of overall energy demand with a decrease in consumption of fossil fuels. Among others, photovoltaic technologies represent one of the most promising answers, and this effervescent research field is in constant expansion, with the goal of developing more and more efficient devices.

The efficiency of a photovoltaic device can be increased by the identification of new active materials, or by building a progressive and comprehensive knowledge about how these materials work in a specific device architecture. Among the most recent advancements in the field, the employment of halide perovskites represented a breakthrough. These materials have recently come in the spotlight for record power conversion efficiencies as photo-active layers in solar cells, but they proved also to possess extremely interesting emission properties for applications as light emitting devices and lasers. Before entering in details for the specific case of perovskite-based photovoltaics, a more general introduction over the physics behind solar-to-electrical energy conversion is given.

1.1 The physics of solar cells

The solar cell is an optoelectronic device able to convert light photons into electric current. The electro-magnetic radiation emitted by the Sun spun over the entire spectrum of frequencies of a black body with a temperature of 5777 K [1]. Only a fraction of this radiation reaches the surface of the Earth. The *air mass coefficient* (AM1.5) is an index used to determine the effective electromagnetic radiation emitted by the Sun at the sea level [2]. The main losses with respect the pristine emission are due absorption by chemical components of the Earth's atmosphere, like ozone, water, oxygen

and carbon dioxide. These molecules absorb a relevant part of the spectrum emitted, preventing ultraviolet (UV) and some parts of the infrared (IR) portions of the solar spectrum to reach the surface of the planet. The AM1.5 spectrum represents the maximum amount of energy available for a solar cell to be converted in electrical current.

A solar cell can be pictured as a «black box», in which light goes in and electrons go out. In principle all the different kind of solar cells must respect these characteristics [1]:

- ▷ Being able to absorb the incoming photons. The absorption process is determined by the atomic and molecular composition of the material. An ideal candidate core material for current generation in a solar cell has an absorption spectrum that matches the AM1.5 spectrum.

- ▷ Being able to generate charges. Upon light absorption, generation of photo-carriers must follows. There are several mechanisms through which the photo-generation can occur. The nature of this process itself defines the type of solar cell.

- ▷ Being able to transport charges. Once the charges are generated, the device must be able to collect them, because without any driving force the photo-generated species will recombine. The architecture of the solar cell must provide an internal electric field, defined as *built-in* field, which guarantees the collection. The optimization of the structure, with the engineering of the core active material or the inclusion of other interlayers is the core of the advancement in the photovoltaic field.

A brief overview of the technology evolution in the photovoltaic world can be divided in four parts, as clearly reported in Fig. 1.1 [10]. The «first generation» of solar cell devices were based on ultra-pure silicon wafers. The main problem for this technology was the requirement for high volume of active materials. A «second generation» of solar cells was developed starting from the early 80s, with the employment of thin film semiconductors. Regardless of the chemical nature of the active material involved, thin-film technology offers the great advantage of the cost reduction, by minimising the quantity of material used. In the 90s, a novel paradigm entered the research: new types of solar cells that exploited alternative mechanisms of energy conversion, mimic the photosynthesis. This latter type of technology is represented by the so called «third generation» solar cells. Overall, the most performing technology is the multi-junction solar cell, in which a stack of different semiconductors is employed, in order to match perfectly the solar spectrum. This match, and the related impressive efficiency, comes to the cost of extremely expensive engineering of the devices, or bulky concentrator systems (cite). In the last years, emerging photovoltaics are attracting more and more interest

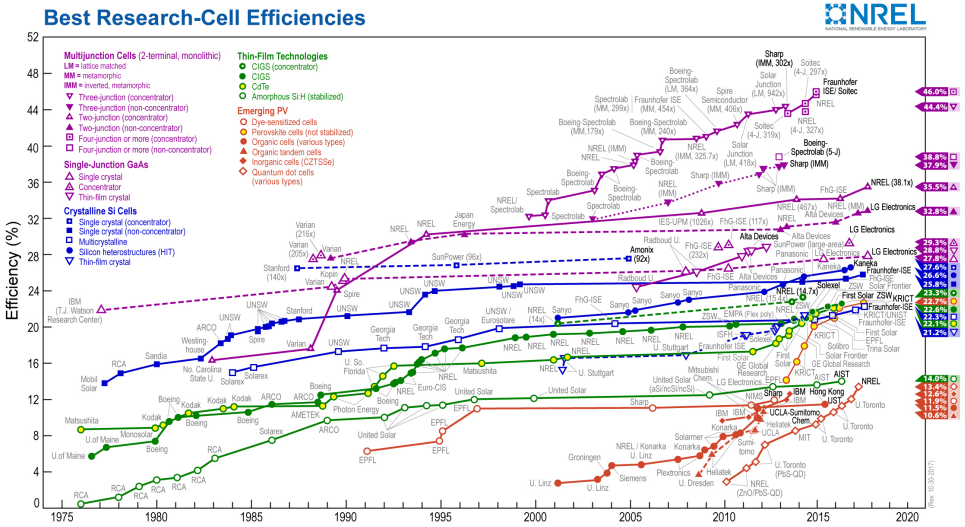

Figure 1.1: Reported timeline of best research solar cells energy conversion efficiencies from 1975 up to today. Reproduced from [10].

due to their potential cost-benefits and their adaptability for a broad range of advanced applications, from an alternative to reduce the cost of multi-junction solar cells, to the use of flexible substrates. Even if the resulting efficiencies are not as high as mono-crystalline silicon, many of these new materials can be processed from solution, with techniques that may drastically lower the cost of production. These devices can be realized with industrial printing techniques, such as roll-to-roll, slot dye coating, ink-jet printing and bar coating processes, and thus are potentially scalable to high throughput productions. In this category, many promising photovoltaics systems are included: perovskite-based materials and inorganic quantum-confined nanocrystals. It has to be mentioned that this class comprehends organic photovoltaics, in which organic polymers and small molecules are employed as active layers for light absorption and charge transport. These technologies have attracted a lot of research interest mainly due to the promising properties of the final devices: the solar cells can be made flexible, light in weight and semi-transparent, paving the way fot building-integrated systems and portable electronics [3]. A major limitation of this novel class is mainly represented by the long term stability, that has to compete with the silicon-based devices ($>$ 25 years).

1.1.1 Characteristics of solar cells

The solar cell can be compared to a battery inserted in a simple electrical circuit. When the cell is illuminated, it develops a photo-voltage. If the two terminals of the cell are isolated, as with an infinite load resistance, the

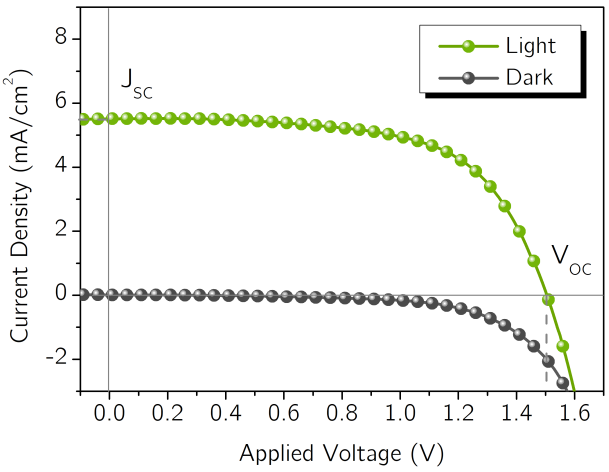

Figure 1.2: Current-Voltage characteristic of a real device, exposed to light (green dots) or measured in dark (grey dots). Approximately, the net current is obtained by shifting up the bias-dependent dark current, by a constant amount equal to the short circuit current (J_{SC}). The sign convention is such that the photo-generated current is positive.

voltage created is defined as *Open Circuit Voltage* (V_{OC}). When the two terminals are connected together, the current, generated under illumination, is denominated *Short Circuit Current* (I_{SC}). For a given load resistance, R_L, the cell provides a current I(V) according to Ohm's law, for which $V = I \cdot R_L$, for voltages between 0 and V_{OC}. Moreover, since the generated current is proportional to the illuminated area, the more useful parameter of *Short Circuit Current Density* (J_{SC}) is employed, a normalized value over the active area of the cell. J(V) defines the *Current-Voltage characteristic* (J-V curve, see Fig.1.2) of the solar cell. An ideal solar cell behaves in dark like a diode, with a different current under forward applied voltages ($V > 0$) respect to reverse bias ($V < 0$). The rectifying behaviour is a feature of photovoltaic devices, and it is a consequence of an asymmetric junction that is needed to separate charges. Upon illumination, the J-V characteristic is shifted up by a factor proportional to the short circuit current. Electrically, the photo-current produced by the device is divided between the variable resistances of the diode and of the load applied. In the range of voltages from 0 to V_{OC} corresponds to the working region of the device, thus within this range the cell delivers power. The power density of the cell, defined as $P = V \cdot J$, shows the following properties (see Fig.1.3):

1. The maximum value P_{MAX} is defined as the *maximum power point* (M_{PP}) of the cell, in which the product $P = V \cdot J$ is maximized. For this value, it is possible to define V_M and J_M. Subsequently, the optimum load for a solar cell has a resistance given by V_M/J_M.

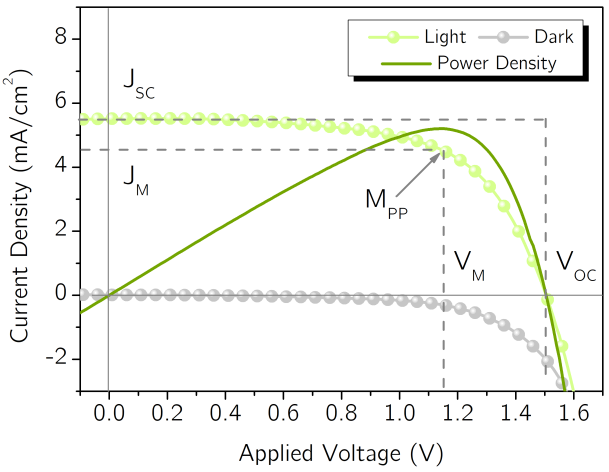

Figure 1.3: The maximum power density $V_M \cdot J_M$ is given by the area of the inner rectangle. The area $V_{OC} \cdot J_{SC}$ is the outer rectangle. The FF is the area of the largest rectangle which will fit in the JV curve.

2. From V_M and J_M it is defined the so-called *fill factor* (FF), a parameter used to describe the «squareness» of the J-V curve. In fact, FF = $V_M \cdot J_M / V_{OC} \cdot J_{SC}$.

3. The efficiency of a cell is expressed by the power delivered at the maximum power point as a function of the incident light power density (P_{in}), and it is called *power conversion efficiency* (PCE).

$$PCE = \frac{J_M \cdot V_M}{P_{in}} = \frac{J_{SC} \cdot V_{OC} \cdot FF}{P_{in}} \tag{1.1}$$

4. The parameters J_{SC}, V_{OC}, FF and PCE and are the figures of merit of a solar cell. These must be defined under standard illumination conditions, employing the AM1.5 spectrum of an incident power density of 1000 W/m^2.

1.1.2 The physics of semiconductors

The nature of the band gap in a material is related to its atomic characteristics. The electrons of an isolated atom occupy atomic orbitals, characterized by a specific energy level. When two atoms form a molecule, their atomic orbitals overlap. According to the *Pauli exclusion principle*, in a molecule, two electrons can not have the same quantum numbers. So, each starting atomic orbital splits into two molecular orbitals of different energy, allowing the electrons in the former atomic orbitals, to occupy the new molecular orbital without breaking Pauli's principle. This can be repeated indefinitely,

as for a solid, in which a large number (N) of identical atoms come together, in a crystal lattice. Since the number of atoms in a macroscopic piece of solid is a very large number ($N \approx 10^{22}$) the number of new orbitals is very large, and these are very closely spaced in energy. The splitting, in fact, will be in the order of 10^{-22} eV. The energy of two adjacent levels will be so close that they can be considered as a continuum, the so-called *energy band*. Band-gaps are essentially ranges of energy not covered by any band, as a result of the finite widths of the energy bands. The width of a band can be very different, depending upon the degree of overlap in the starting atomic orbitals. The separation in energy between the two bands, expressed in eV, determine the type of material: metals (0 eV), semi-metals (less than 0.5 eV), semiconductors (between 0.5 and 3 eV) and insulators (more than 3 eV). In a very simple way, with the term *generation* is identified any electronic excitation event which increases the number of free carriers available in a material. In this sense, any *recombination* is an electronic relaxation event in which the number of available free carriers is reduced. The generation process requires the absorption of energy quanta, either vibrations of the lattice (*phonons*) or electro-magnetic radiation (*photons*). The recombination releases energy as the same quanta, as the inverse mechanisms of generation. As above mentioned, in a solar cell the charge-carrier generation is guaranteed by light absorption and it is called *photo-generation*. Without a band gap, like in metals, the excited electrons don't have enough time to be collected: the carriers would decay through a continuum of intermediate levels. In the presence of a band-gap, after the excitation event, they quickly decay to the minimum energy of the upper band, the so-called *conduction band* (CB), within few femto-seconds. The recombination to the lower band, *valence band* (VB), will occur afterwards with a slower timescale compared to the first one, up to about several micro-seconds, giving enough time to the solar cell to extract the carriers. When an electron is promoted from the VB to the CB, a positively charged vacancy remains in the VB. This vacancy is usually filled by the near electrons in the VB, moving the vacancy to the neighbour site. In the presence of an electric field, this process can be repeated resulting in a photo-generated current given by the movement of the vacancy in the opposite direction to the promoted electron. Since this vacancy results from a lack of negative charge, it can be described as a current of positively charged holes in the VB. The electron and the relative hole are charges with opposite signs. Depending on the photo-physical characteristics of the material, these two charges can be independent or strongly interacting. In specific conditions the Coulomb interaction, manifested between the two different charges, bind the photo-generated carriers in a unique state, called *exciton*. They result in a series of intra-band gap states slightly above the VB and below the CB. These excitonic states can play a major role in determining the opto-electronic properties of semiconductors.

1.1.3 Generation and recombination mechanisms

The principle of detailed balance for carrier generation and recombination processes imposes radiative recombination within a semiconductor [27]. At the same time, photo-generated free carriers may recombine through additional mechanisms. Whether a particular recombination mechanism is relevant, for a given excitation density and given temperature, is dependent on the densities of the carrier population and on the statistics of carrier interactions with the defect states in the band-gap. When a structural defect energetically lies within the semiconductor band-gap, a chance that an excited species will be captured by it is different from zero. The trapped carrier is likely to be emitted back to the band by phonon absorption if, and only if, the activation energy of the de-trapping process is sufficiently small. However, if this energy is large, it is likely that the trapped carrier will annihilate, recombining with the opposite carrier before it can be re-emitted. The rate of every recombination processes can be determined by the Shockley–Read–Hall (SRH) statistics. At low excitation densities, the photo-excited population decays with a mono-molecular rate. As the photo-excitation density increases, this decay channel saturates, and bimolecular band-to-band recombination between free electrons and holes increasingly contributes to the overall recombination rate. At much higher densities, three-body interactions become probable and Auger recombination becomes preponderant. The time-dependent behaviour of the carrier population can be described with a rate equation that accounts for all these processes, as:

$$\frac{dn}{dt} = -k_{\mathrm{Auger}} n^3 - k_{\mathrm{rad}} n^2 - k_{\mathrm{t}} n$$

where n is the excited carrier density, and k_{t} , k_{rad} , and k_{Auger} are the rate constants for, respectively, mono-, bi-molecular and three-body recombination. These rates can be experimentally determined by time-resolved photoluminescence decay and pump-probe spectroscopy. In solar cells, defect-mediated non-radiative carrier recombination is of fundamental importance under open-circuit conditions. In fact, under steady-state illumination, electrons are photo-excited from the valence to the conduction band, splitting the electron and hole quasi-Fermi levels. The charge density at which the recombination rate equals the generation rate determines the difference in quasi-Fermi levels. All the additional non-radiative recombination processes that have a shorter lifetime than the radiative one reduce the steady-state charge density. Thus, the gap between quasi-Fermi levels will be reduced, and the value of the open-circuit voltage will follow it.

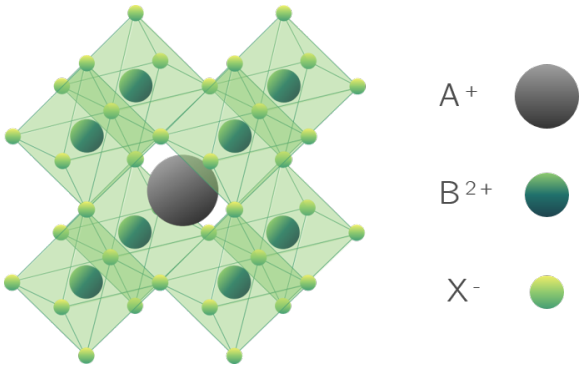

Figure 1.4: A representation of the tri-dimensional perovskite crystal structure (in the cubic phase), comprehending more than one unit cell. B cations (dark green) assembled around X anions (light green) to form BX_6 octahedra. The octahedra share all their corners, creating a «cage» in which the A cation is confinated.

1.2 Perovskites

A German mineralogist, Gustav Rose, discovered in 1839 the calcium titanate mineral ($CaTiO_3$), and few years later, its crystal structure was named after the Russian mineralogist Lev A. Perovski. This crystal structure was first described and characterized by Victor Goldschmidt, in 1926. Then, it lent its name to a more broad class of compounds, now known as *perovskites*, which share the same type of crystal structure, represented by the general chemical formula ABX_3. A and B stand for cations of different size, while X are anions, typically oxygen or halogens. Historically, oxide-based perovskites (in which X = Oxygen) have been the most studied of the family, as a result of their intriguing ferroelectric, magnetic, and superconductive properties [4]. The first to report in literature a lead-halide based perovskite was Møller, in 1958, investigating the photoconductive properties of $CsPbX_3$ perovskite [5]. The first appearance of organic cation lead-halide perovskite was in 1978, in the work by Weber and Naturforsch [6]. But it was not until Kagan and Mitzi, the end of the 20^{th} century, that the perovskite were introduced in electronic devices as semiconductors. These pioneering works demonstrated the possibility to employ layered organic-inorganic halide perovskites as the active phase in light emitting diodes (LEDs) and thin film transistors (TFTs) [7], [8]. Later on, Miyasaka and coworkers introduced methylammonium lead bromide (A = CH_3NH_3, B = Pb and X = Br) as sensitizer in a photovoltaic device, in 2006. The power conversion efficiency (PCE) obtained was 2.2% [8]. Over the past few years, the PCE of perovskite solar cells (PSCs) increased from 3.8% [9] to 22.7% [10], surpassing the well-studied organic-based dye-sensitized solar cells and rivaling the established technologies based on CdTe, Si, and copper indium gallium selenide devices. Currently, lead-halide perovskite is regarded as the most promising photo-

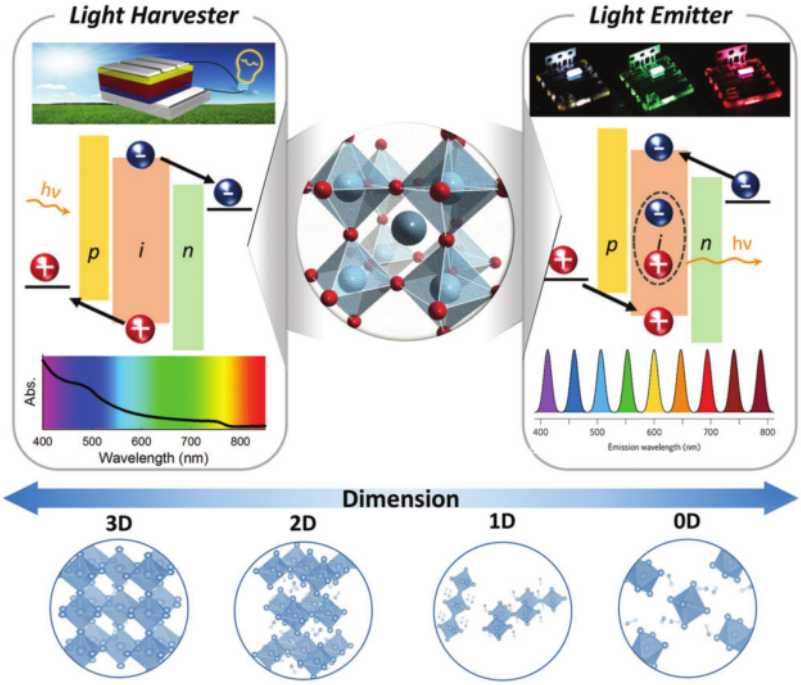

Figure 1.5: Schematic description of representative optoelectronic applications of hybrid perovskites a guide arrow for dimension control for different target applications. On the left, perovskites for light harvesting, while on the right, the materials for light emission. The dimension of the A cation can tune the coordination of atoms in the final lattice (nD), going from tri-dimensional to zero-dimensional structures. Copyright 2015, American Chemical Society.

voltaic technology for the next generation of solar cells. This is due mostly to the optimal optoelectronic properties showed by these materials, such as high charge-carrier mobility and large spectral tunability of the absorption coefficient, together with the low cost solution-process deposition.

1.2.1 Crystalline structure

In this section we briefly present the structural properties of the lead-halide perovskite (from now on, PVK) crystal.

In the case of hybrid perovskite the A site is occupied by an organic species. The most widely used in the past years is the Methylammonium ion $CH_3NH_3^+$ (MA), however more recently also Formamidinium $CH(NH_2)_2^+$ (FA), Cesium (Cs) and Rubidium (Rb) have been widely and successfully employed. The X site is occupied by an halide anion. The B is a metal cation from the IVA group in a divalent oxidation (Pb^{2+} or Sn^{2+}). In this thesis we will consider only the case of lead-halide PVK. This choice is dictated by the fact that, up to now, lead has proven to be superior with respect to tin, both in terms of performance and long term stability. Anyway, an entire sector of

the research community is focusing in replacing lead with less toxic species, as demonstrated by some preliminary results from Noel et al.[11] and Hao [12]. The size, shape and charge distribution of the A cations relatively to the B atom are of paramount importance for the stability of the structures. The ideal symmetry of the 3D crystalline structure is a face centered cubic cell, consists of corner-sharing $[BX_6]^{4-}$ octahedra, in which the A cations occupy the voids existing between the adjacent octahedra. Goldschmidt introduced a tolerance factor, t, to predict the stability and distortion of the crystalline structure of PVK materials [13]. This factor is expressed by the formula:

$$t = \frac{r_A + r_X}{\sqrt{2}(r_B + r_X)}$$

in which r_A, r_B and r_X represent respectively the ionic radii of the A, B and X species. In general, PVK materials with a t value between 0.91 and 1.0 prefer a cubic PVK structure [14], [15]. While, a value for t ranging from 0.71 to 0.90 corresponds to a tetragonal or orthorhombic structure. Given this range of t, the ionic radii of chosen organic cations should be limited to 2.9 Å, considering the ionic radii of Pb (1.2 Å) and I (2.2 Å). This reduces the choice to organic molecules with fewer than two or three C-C and C-N bonds [16]. Otherwise, low-dimensional PVK crystalline lattices are obtained, as will be discussed. In terms of electronic properties, the valance band maximum of a PVK material is composed of anti-bonding state between B-s and X-p orbitals, while the conduction band minimum is determined by a non-bonding state between B-p and X-p orbitals [17]. The size of the A ion does not directly affect the overall electronic structure of the perovskite but it influences crystal symmetry by the distortion of BX_6 octahedra, or it induces a variation in the dimensionality of the final lattice [18]. Enlarging the size of the A cations, the structural dimensionality of halide perovskites can be easily tuned, to obtain two-, one- or zero-dimensional PVK lattices. These PVK possess different photo-physical and electronic properties compared to the conventional tri-dimensional counterparts. They show larger band-gap and higher excitonic binding energy [20], that grows correspondingly to the size of cations. The band-gap of 2D crystals can be tuned through tailoring the number of inorganic layers (n value, as show in Fig.1.5). Among the advantages of these lower-dimensional materials, it has been demonstrated that these material can show a slower rate of degradation of the device performances under high umidity conditions. However, the directionality of metal halide lattices in 2D perovskite usually imposes limitations in charge transport and extraction, contributing to the lower efficiencies obtained, compared to the ones given by the tri-dimensional counterparts [19].

1.3 Optoelectronic properties of perovskites

The core of optoelectronic applications is the management of light, such as absorption, transmission, emission and modulation, and it is governed by the quantum-mechanical properties of optoelectronic materials. Thus, the electronic structures of the semiconductors, as the optical band-gap and density of quantum states, along with the characteristics of exciton, carrier lifetimes and mobility, are significant parameters for opto-electronic materials. The wide tunability of the perovskite electronic structures enables the realization of various opto-electronic devices such as solar cells, light-emitting diodes, photodetectors, and lasers. In the following subsections, the basic opto-electronic properties of the PVK-based materials are discussed.

1.3.1 Energy band-gap and chemical composition

The band-gap of an organic-inorganic hybrid perovskite is in the visible range of the light spectrum (1.2-3.0 eV). Moving down in the VIIA group of the periodic table, the halogen ionic radius increases. Once incorporated in a PVK structure, this will affect the electronic distribution, inducing a red-shift of the absorption onset of the material. This translates in a reduction of the semiconductor band gap [22]. For example, according to the $MAPbX_3$ composition, the band gap is widely controllable from 1.55 to 3.11 eV, along with the halogen substitution. In this section, a summary of the state-of-the-art results concerning the technology based on different cation and different halide PVK is reported.

◇ **Pure iodide perovskites** For photovoltaic applications, the iodine based lead-halide materials have shown unrivalled superiority with respect to the pure chlorine and bromine-based counterparts. The band-gaps of the mostly widely used PVK light harvesters, such as $MAPbI_3$ (1.55 eV) and $FAPbI_3$ (1.43-1.48 eV) are close to the desirable optimal value of 1.4 eV, as suggested by the Shockley-Queisser efficiency limit [27]. Among them, $MAPbI_3$ is the prototypical absorber material for PSCs. Though the PCE of the devices based on $MAPbI_3$ reaches 20%, several intrinsic characteristics of this material hinder its industrialization. The first and most critical one is related to its instabilities. These comprehend thermal, electrical and moisture instabilities [17], [23], [24], [25], [26]. Second, the $MAPbI_3$ absorber shows a high absorption coefficient only for photons above 800 nm, which impede the further improvement of PCE. The formamidinium ion, with an ionic size of 2.2 Å, is slightly larger than MA (1.8 Å). $FAPbI_3$ possess a bandgap of 1.48 eV, which allows for the collection of photons in near infrared (NIR) range in PV devices. Angelis and co-worker's calculations have concluded that $FAPbI_3$ exhibits improved charge transport properties compared to $MAPbI_3$ [28]. However, $FAPbI_3$-based PSCs display inferior photovoltaic performance due

to an undesirable phase transition from the black PVK phase (α-$FAPbI_3$) to a yellow photo-inactive phase (δ-$FAPbI_3$) at room temperature [29], [30]. The pure inorganic iodide PVK, $CsPbI_3$, exhibits excellent thermal stability [31], however, as $FAPbI_3$, the stable phase for this material is the orthorhombic alpha-phase, not suitable for PV application. The photo-active phase is only stable at temperatures higher than 300°C [5]. Moreover, in this case the band-gap increases to 1.73 eV, moving away from the optimal value reported previously. These two factors, i.e. the phase instability and the not-optimal band-gap of the pure iodide materials, are the main reason for the growth of a new branch of the research field in perovskite, which focuses on the investigation of mixed-halide and/or mixed-cation alternatives.

◇ **Mixed-composition perovskites** The mixed PVK have become now-a-days an important approach to achieve highly efficient and more stable solar cells. The highest PCE of PSCs reported so far, in fact, come from PVK materials with composition in which both cations and halides are mixed. Before the discussion, it is noteworthy that the reported compositions of the solution-processed films usually refer to the molar ratio of elements in the precursor solution, rather than the actual composition in the final material. The mixed PVK include mixing of individual sites (A, B, and X sites) and mixing of multiple sites (as known as double or triple PVK). For sake of clarity, the various alternatives will be presented as they have been discovered in literature.

1. X-site mixed perovskites The common X site occupant is a halide anion, such as Cl^-, Br^- and I^-. Due to their electronic states, the halide species have great influence on the valence band energy. For example, going from Cl to I, the valence band changes, and meanwhile, the electron binding energy decrease [50]. As a result, the valence band of the chloride-based PVK is 0.6 eV higher than the iodide-based one [51].

1.a ◇ Cl-I mixture. Starting from the pioneering work by Lee et al., the Cl species incorporation within $MAPbI_3$ was regarded as one of the main route towards highly efficient PSCs [52]. The adoption of $PbCl_2$ to replace PbI_2 generated the mixed halide compounds of $MAPbI_{3-x}Cl_x$. Devices with this configuration initially delivered a PCE of 10.9%. The mixed halide PVK act as an electron transporter and light absorber which demonstrate better light harvesting abilities than the $MAPbI_3$ prepared with PbI_2. Despite the presence of Cl^- in the precursor, the chlorine is not able to be observed in the resulted films [53], [55], [54]. Research efforts focused on the lost of Cl^-, and Yu et al. proposed that most of Cl^- was released in the form of MACl gas [56]. They suggested that the excess of MACl is beneficial to form larger crystal domains. This is due to the slower crystal lattice formation process. Moreover, the larger grain size would effectively decreased the number of

grain boundary per area, enabling the charge carriers to move across the films in a single-crystal-like environment, reducing charge recombination [57]. The addition of Cl improved the film morphology, and this guaranteed better device performances.

1.b ◇ Br-I mixture. Analogous to Cl^- doping, the introduction of Br^- during thin film fabrication can also enhance film quality [32]. In the perspective of crystallography, at RT, $MAPbI_3$ is tetragonal while $MAPbBr_3$ presents a cubic structure [33]. Therefore, gradually replacing I^- with Br^- also increases the symmetry of the lattice. Furthermore, the conversion from tetragonal structure to the cubic one enhanced the device stability against humid environment. It is well known that $MAPbI_3$ is susceptible to moisture: upon ambient exposure the film rapidly deteriorates into PbI_2. The Br-doped sample was demonstrated better humidity stability, and could still deliver higher PCE even after 20 days at relatively high humidity ($\geq$55%), in respect to the un-doped sample [34]. In addition to improving film morphology, the incorporation of Br^- has a significant impact on the band-gap of the final film. It has been reported that the substitution of I^- with Br^- will cause the phase segregation in the resultant films, which decreases the device overall performance [35], [36]. The Open-Circuit Voltage (V_{OC}) decreased in the $MAPb(Br_xI_{1-x})_3$ based devices with the increasing amount of Br^-, when the content exceed 20%. This issue has attracted an incredible amount of research efforts. Hoke and co-workers studied the PL spectra of the mixed Br-I PVK and observed the PL spectra evolution along with the time. Upon constant illumination, the XRD peaks split. They concluded this was a result of light-induced phase segregation into iodide- and bromide-rich phases [35]. Interestingly, the photo-induced process is reversible: when relaxed in the dark, the film reverted back to its original single-phase state. They suggested that photo-generated polarons induce a local strain, which assists halide phase separation, and results in the formation of I-rich clusters. This was one of the first evidences that suggested halogen motion in the crystal lattice. McGehee et al. speculates this ion migration strongly linked with the Current-Voltage hysteresis [36]. Recent research has demonstrated that halide migration is promoted by halogen vacancies [58] and migrated faster at the grain boundary compared to that of the grain interior [59]. This implies that reducing grain boundary density maybe an effective way to alleviate phase separation. Very recently, Barker et al. found that this segregation may be driven by the strong gradient in carrier generation rate through the thickness of these PVK, which are strongly absorbing materials [60]. Moreover, it has been shown that the Br^- ions move more rapidly compared to the I^- ones. Once returned to the dark, entropically driven intermixing of halides returns the system to a homogeneous condition. In order to suppress this effect, they suggested to control either the internal light distribution or the defect density within the film. These results are extremely relevant to reach the stability in both single- and mixed-halide perovskites, leading the

way toward tunable and stable perovskite thin films for photovoltaic and light-emitting applications.

2. *A*-site mixed perovskites Mono-*A*-cation PVK generally suffer from thermal or structural instabilities, or imperfect band-gaps. To achieve improved stability and more suitable optoelectronic properties, mixture of FA^+ with MA^+ or Cs^+ have proven a feasible solution. Pellet et al., in their pioneering work, proposed the use of $MA_xFA_{1-x}PbI_3$ in mesoscopic PSCs. In the paper, a detailed analysis on the structure, electrical, and optoelectronic properties of the mixed material is reported [41]. They showed that the undesirable δ-$FAPbI_3$ could be completely avoided when $x = 0.2$, while the band-gap of pure $FAPbI_3$ was maintained. The best photovoltaic performance was obtained for a ratio of $MA : FA = 0.6 : 0.4$, with a PCE of 14.9%, due to the higher harvesting efficiency of light in longer wavelength regions. After this seminal work, several works followed. Han et al. developed a novel strategy for fabricating pure-phase $MAxFA_{1-x}PbI_3$ from a a non-stoichiometric intermediate $(FAI)_{1-x}$-PbI_2, showing overall improved performances compared to $MAPbI_3$ [42]. Snaith et al. developed a facile cation exchange approach for the interconversion between $MAPbI_3$ and $FAPbI_3$, in order to obtain mixed-organic-cation films by a simple dip coating step in isopropanol solution of FAI or MAI at room temperature [43]. By optimizing the cation exchange reaction time and process, the hybrid PVK solar cell performance can be significantly enhanced. Similar to MA, incorporation of Cs^+ into FA-based materials can also enhance the stability of α-$FAPbX_3$. Li et al. found that by introducing moderate amount of Cs^+ into $FAPbI_3$ the PVK displayed a more stable phase, and accordingly, the PSCs showed increased device stability compared to their pure $FAPbI_3$ counterparts [44]. Similarly Park and co-workers, showed that the photo and moisture stability of $FA_{0.9}Cs_{0.1}PbI_3$ films were improved significantly. Furthermore,upon incorporation of Cs^+, trap density was reduced resulting in enhancement of average PCE from 14.9% to 16.5% [45].

In addition to the double-cation PVK, materials with more complex compositions were studied to further increase device efficiency, such as the triple or quadruple cation PVK. Saliba et al. were the first to employ the triple cation PVK (with a mixture of halides too) $Cs_x(MA_{0.17}FA_{0.83})_{100-x}Pb(I_{0.83}Br_{0.17})_3$ as active layer. The resulting films were more thermally stable and less sensitive to processing conditions, which enabled more reproducible devices. They achieved stabilized PCE of 21.1%, dropped to 18% after 250 hours under operational conditions [38]. Then, they introduced Rb^+, considering that the ionic size of this ion is slightly smaller than Cs^+ [39]. PSCs based on this quadruple cation PVK showed a stabilized PCE of 21.6% on small areas. More importantly, after the coating with a thin layer of poly-triarylamine polymer, the solar cells could maintain 95% of their initial

efficiencies, operating at 85°C for 500 hours.

3. *B*-site mixed perovskites *B*-site mixed PVK are formed by introducing other metal cations into crystals. The well-known toxicity of Pb^{2+} limits the lead-based PVK technology industrial application potential. Thus, the development of lead-free material without sacrificing the device performance is attracting a lot of interest. Among the candidates, Sn^{2+} is an excellent selection to completely or partially replace Pb, since the ionic radius of Sn^{2+} is very close to the lead. In recent years, $CsSnI_3$ or $MASnI_3$ were studied as lead-free light absorbers [46], [47], [48]. However, low PCE have been obtained compared with Pb-based PSCs due to the easy oxidation of Sn^{2+} to Sn^{4+}, which results in structural changes and consequently metal-like conductivity [49].

4. Dual/triple-site mixed perovskite Motivated by the need to improve stability and PCE of PSCs, more complex combinations of ABX_3 hybrid organic-inorganic PVK have been explored, namely, mixed-*A*/mixed-*X*, mixed-*A*/mixed-*B*, mixed-*A*/mixed-*B*/mixed-*X* materials. The multi-site mixed PVK are of interest mainly due to two motivations: to enhance both stability and efficiency, for commercialization, and to tune the band-gap for tandem applications. Eperon and co-workers combined a 1.2 eV mixed-cation tin PVK with a wider band-gap material, with a mixed-cation mixed-halide lead PVK, obtaining two-terminal and four-terminal tandem solar cells with an efficiency of 17.0% and 20.3%, respectively, with impressive stablity in compare to the pure-Sn-based counterparts [40]. Anyway, though these combinations show the highest PCE, a deep understanding regarding the microscopic elemental distribution of these multi-site mixed solid solution films is missing, which is crucial for device optimization.

1.3.2 Photo-generated carrier behaviour

Optoelectronic devices rely on the behaviour of excitons generated by external stimulation of the semiconducting materials, such as light absorption or external bias. An exciton is defined as a neutral quasi-particle composed of bound electron–hole pair by electrostatic Coulombic attraction [61], [62]. Representative types of excitons are identified as *Wannier–Mott* type excitons (binding Energy, E_b, ≤ 0.1 eV) and *Frenkel* type excitons ($E_b \geq 0.1$ eV) [63]. The understanding of photo-generated carriers behaviour in a PVK material is crucial for the exploration of these as promising optoelectronic active components. The first two years of research activities saw a major debate on this topic. It was unclear whether, upon photon absorption, the generated carriers existed as bounded excitons or free electrons and holes pairs. It is now accepted that PVK harvester-materials spontaneously generate free electrons and holes, which is the main reason to the impressive performance

in PV technology [64]. This is due to the low E_b that characterize these materials at RT, that ranges from 2 to 50 meV, compared with thermal energy of $k_{BT} \approx 25$ meV [65]. In addition to the chemical composition, the E_b value can be considerably altered depending on the crystal size and film morphology [66]. Beyond the interest in PSCs, that are based on light absorption, the focus on exploitation of light emission from these materials is increasing. In simple terms, while a solar cell requires low E_b for efficient generation of free electron and holes, for a *light-emitting diode* (LED) a tightly bound exciton is needed for efficient radiative decay. The management of the crystalline structure and dimensionality of the PVK lattices has been proven to enable a broad distribution of exciton binding energies, ranging from 2 to a few hundred meV. Independently from the technological application the research is targeting, a deep understanding of the photo-physical mechanisms behind the charge generation, recombination, transport and collection is essential. Specifically, an accurate analysis of the evolution of the photo-generated species is needed: the efficiency in radiative recombination (i.e., the *photoluminescence quantum yield*, PLQY) can be related to the structural quality of the perovskite lattice, as it will be discussed in the next sections. Thus, one of the main goals for the researchers in the field is the development of synthesis protocols that can guarantee the growth of nearly perfect perovskite lattices. Changing the parameters involved in the early synthetic steps can have a huge impact on the quality of the crystals, that can be investigated through a PLQY analysis.

1.4 The role of the crystallization process

The organic and inorganic components of the PVK materials facilitates low-temperature solution processing. Thus, the crystallization process has a major influence over the subsequent photovoltaic performances and stability. Control over morphology is a key parameter to obtain high-performance optoelectronic devices, and an additional step to be taken throughout the commercialization process. In the following pages, several parameters influencing the perovskite morphology due to different crystallization mechanisms will be discussed.

1.4.1 Deposition methods

1. One-step depositions In the initial stage of hybrid perovskite research for optoelectronics, a single-step spin-coating method was the main deposition technique used to obtain thin films [67]. Although spin-coating is an apparently simple method, the interactions between metal cations and halogen anions usually leads to the formation of inhomogeneous morphology, completely unsuitable for device application. In particular, the films obtained showed pillared structure, very poor surface coverage [68], and

non-uniform film thickness [85]. Commonly, this step involves a precursor solution made of MAI and PbI_2 powders dissolved in polar solvents such as dimethylformamide (DMF), dimethyl sulfoxide (DMSO) or gamma-butyrolactone (GBL). In 2014, the *anti-solvent dripping* method was developed for highly uniform and homogeneous perovskite film formation. Anti-solvents such as toluene and chlorobenzene, are dripped during the spinning of precursor solutions [68], [70]. This simple approach results in homogeneous perovskite layers over large area, that show enhanced performances. The method relies on two combined factors: i) the creation of chemical complexes inside the precursor solution, prior to the deposition; ii) the dripping of a specific anti-solvent during the spin-coating step. In the case of precursor solutions containing dimethyl sulfoxide (DMSO), kinetically frozen uniform layer of MAI-PbI_2-DMSO is formed as an intermediate phase. Anti-solvent dripping is known to induce rapid supersaturation of perovskite precursors, thus it promotes a fast nucleation and growth of densely packed grains. Solid-state conversion from the intermediate phase film to perovskite film by thermal annealing yields remarkably uniform perovskite films thanks to the delayed reaction between the organic and inorganic precursors. The type of anti-solvent, dripping timing, and spinning rate are key factors influencing the final perovskite film morphology. Benzene derivatives, diethyl ether, and chloroform are reported to be effective anti-solvents for selective washing of DMF with high reproducibility [71], [72]. Ahn et al. investigated the formation mechanism of the solvent-meditated intermediate phase [73]. To date, all the most performing solar cell devices are prepared following this method. Moreover, such devices demonstrate highly reproducible performance with the best PCE of 21.6% [39].

2. Two-step depositions In contrast to the single-step spin-coating from pre-mixed organic and inorganic precursor solution, perovskite can be synthesized by a sequential deposition of separated inorganic and organic components, called two-step process [74]. The inorganic component is deposited prior to organic species. The contact between these two components initiates the phase transition to the perovskite structure. The thermal annealing that follows completes the perovskite lattice formation by the inter-diffusion of two components. In this category, a great number of different deposition methods can be found. The very first to be optimized has been the dual source evaporation of organic and inorganic components, which enables the formation of highly crystalline perovskite over large area with superior homogeneity. In the report by Liu et al. [42], vapor evaporation of mixed halide perovskite showed more uniform coverage than other solution processes. Another example is represented by the spin-coating step for the inorganic component, followed by the dipping in a solution containing the organic cation. This route has been proven to be extremely useful in order

to be able to control the mean crystallite size, as will be discussed in the next Chapter.

3. Other deposition methods Recently, a wide variety of up-scalable deposition methods have been proposed: among them, slot-die coating, spray deposition and doctor blading of perovskite have been reported as alternatives to the conventional spin coating process. Although these deposition techniques presents several advantages in terms of mass production, the PCE of the devices obtained with these alternatives are still lower than the one produced by the previously discussed techniques. Hwang et al. demonstrated the fabrication of a slot-die coated perovskite solar cells [75]. A pin-hole-free perovskite layer can be obtained by sequential slot-die coating steps with nitrogen gas quenching, with a reduction in the material loss. Spray-coating has also been explored for scalable deposition of perovskite [76], [77]. Doctor-blade coating also offers many attractive features for large area deposition of materials, including low-temperature, simplicity, and compatibility with roll-to-roll fabrication. In 2015, Deng et al. demonstrated a doctor-bladed $MAPbI_3$ perovskite active layer for solar cells [78]. The precursor solution is swiped linearly by a glass blade with a fixed speed, on a pre-heated substrate. The film thickness is controllable by the blading channel and by the solution concentration. Nevertheless, the necessity for thermal annealing and further purification of materials is pointed out as a critical problem to address. Another method has been proposed by Li et al., called *vacuum flash-assisted solution process*, which enables the formation of highly crystalline and smooth perovskite films [79]. A rapid crystallization of the perovskite intermediate phases is promoted by a few second storage of the as-coated films in vacuum (20 Pa). This method allows an excellent infiltration of the active material into the meso-porous scaffold. A maximum PCE of 20.5% has been observed with an active area of 1 cm^2.

1.4.2 Parameters influencing the crystallization

The perovskite film quality, morphology, and material properties are greatly influenced by this step provided that the precursor film is completely wet on a substrate.

1. Heat Thermal annealing has been the mostly widely used method for the crystallization of solution-deposited perovskite precursor films accompanied by the evaporation of residual solvents and additives. The manipulation of heating process variables, including annealing temperature, duration time and substrate pre-heating offers an opportunity to optimize perovskite thin-film by controlling crystalline nucleation and growth kinetics.

Device structure	a	V_{OC} (V)	J_{SC} (mA/cm^2)	FF (%)	PCE (%)	Ref
$MAPbI_{3-x}Cl_x/PC_{61}BM/Bis\text{-}C_{60}$	inv	0.92	17.5	73	11.8	124
$mp\text{-}TiO_2/MAPbI_3/Spiro\text{-}MeOTAD$	std	1.00	22.1	75	16.7	125
$MAPbI_3\text{-}PC_{61}BM/PC_{61}BM/Ca$	inv	0.97	20.2	82	16.0	126
$MAPbI_{3-x}Cl_x/Spiro\text{-}MeOTAD$	std	0.94	19.5	70	13.2	127
$MAPbI_{3-x}Cl_x/PC_{61}BM/Bis\text{-}C_{61}$	inv	0.94	18.5	75	13.1	128
$MAPbI_{3-x}Cl_x/Spiro\text{-}MeOTAD$	inv	0.98	22.9	69	14.8	129
$MAPbI_{3-x}(SCN)_x/PC_{61}BM/Ca$	inv	0.85	17.9	76	11.6	130
$MAPbI_3/PC_{61}BM/Ca$	inv	0.88	14.1	80	9.9	131
$MAPbI_3/PTAA$	std	1.10	20.5	78	17.2	132
$mp\text{-}TiO_2/FAPbI_3/Spiro\text{-}MeOTAD$	std	1.04	18.9	68	13.4	133
$mp\text{-}TiO_2/FAPbI_3/Spiro\text{-}MeOTAD$	std	0.94	23.3	65	14.2	7
$MAPbBr_3/PIF_8\text{-}TAA$	std	1.51	8.4	82	10.4	62

Table 1.1: Effect of the additives on the performances of $MAPbI_3$-based devices, with references. Architectures (a) with c-TiO_2 and Au are labelled with 'std', while architectures with PEDOT:PSS and Ag (or Al) labelled with 'inv'.

2. Additives Appropriate additives can be beneficial for film homogeneity, surface coverage, carrier lifetime, and even device stability. This is due to the direct participation of the molecule into the crystallization process, both during the nucleation and the growth. It can modulates the reaction rate and bonding characteristics. This class of materials includes various organic halide (MACl, FACl, NH_4Cl), organic di-halide (1,8-dii-odooctane, 1,4-diiodobutane), pseudohalide ($Pb(SCN)_2$), acid (HI, HCl, H_2PO_3), and organic small molecules ($PC_{61}BM$, CN), have been investigated to improve the solar cell performance (see Table 1.1 for references). Organic halides, such as MACl, NH_4Cl, and FACl, have commonly been used to improve perovskite film morphology, optoelectronic properties, and even device stability.

3. Vapors Much research effort has been devoted to improve the quality of perovskite films by the manipulation of surrounding environment under solvent vapors including organic solvents, controlled moisture levels, methylamine vapors and vacuum. The most successful method for this kind of treatment is solvent annealing, in which the solvent vapor is introduced during thermal annealing in a closed system [85]. Highly polar solvents make perovskite grains large while the film recrystallizes starting from the surface. Beyond organic solvent or molecule vapor systems, moisture in the atmosphere can affect the film formation [80]. In general, different crystal growth behaviours are observed under different atmospheres, which includes nitrogen, oxygen, and ambient air with a fixed relative humidity [84].

1.5 Defects in perovskite and their effects in solar cells

In more established semiconductors, such as silicon, the control and understanding of defects has been a cornerstone of their technological deployment [81]. Many of the finer details of perovskite halide device physics remain unclear, despite significant research effort. The rate of progress in PCEs for these solar cells is unprecedented, however, suggesting that perovskite halides have a relatively high tolerance for defects. At temperatures relevant for device operation, one could expect a non-negligible level of unintentional defects in the PVK crystal structure, given the simple processability presented earlier. However, although impressive, the highest observed power conversion efficiencies are still far from the thermodynamic limit of 30-33%, for band-gaps in the range 1.2-1.6 eV [27]. In addition, much of the debate in the field surrounding the electrical instability in devices, is concerned with the nature of defects in these materials. Defects, thus, remain one of the interesting material characteristics that determine limitations in device operation, and influence further progress towards reaching the highest PCEs possible. Defects in semiconductors can be either interruptions to an otherwise perfect crystalline lattice or foreign atoms in the structure, as known as impurities. They can be in the form of point defects, such as atomic vacancies, interstitials, and anti-site substitutions, or higher dimensional defects, such as dislocations, grain boundaries, and voids (see Figure 1.6 for a schematic representation). The formation of a given defect within a semiconductor is thermodynamically favourable when its formation energy is negative. This factor is dependent on the atomic and electronic chemical potential: the first is related to the concentrations and activity of reactants, while the second is related to the Fermi level. Thus, the internal defect structure can vary significantly under specific growth conditions, such as different precursor concentrations, temperatures, type of solvent, doping, and more. A key point towards the commercialization of perovskite-based optoelectronic devices is a comprehensive understanding of the defect formation processes and their chemistry. In the following, a brief overview is given of the optoelectronic processes that can be affected by the presence of defects, which will influence device performance metrics. In a solar cell, the active layer thickness should compromise between a maximization of light absorption and an efficient collection of the photo-generated carriers. The collection efficiency is determined by the competition between the processes of recombination and transport towards the contacts. Defects can affect charge transport, because in semiconductors free carriers accelerate through the crystal lattice under an electric field, until they scatter, or interact, with such entities. The mobility of charge carriers is inversely proportional to the carrier effective mass, and proportional to the scattering lifetime. The most

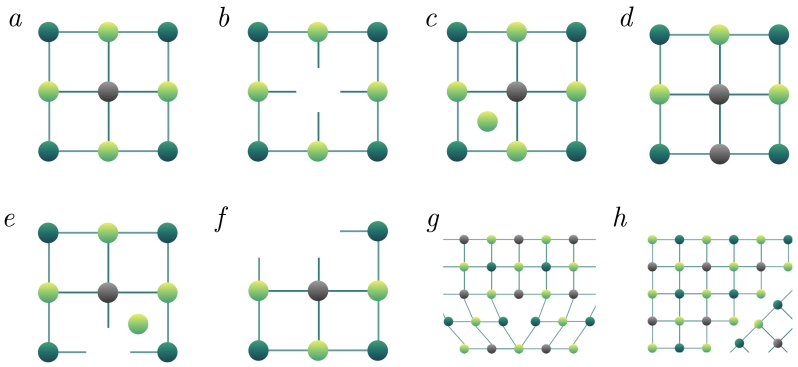

Figure 1.6: Illustration of defects in a perovskite crystal lattice (grey, dark green and green dots represent the A, B, and X ions respectively): a) perfect lattice; b) vacancy; c) interstitial; d) anti-site substitution; e) Frenkel defect, a coupled interstitial and vacancy created from the same ion; f) Schottky defect, an anion and cation vacancies occurring together; g) edge dislocation, a linear defect propagating perpendicularly to the page, and h) grain boundary.

typical interaction between a carrier and a defect is the so called ionized defect scattering: the carrier is deflected by a Coulomb-type interaction. This process shows a temperature dependence. In the extreme limit of highly disordered materials, charge transport becomes dominated by multiple trapping and release process or hopping-like mechanisms [82]. The resulting effective mobility is still thermally activated, but with a limited magnitude. For intermediate trap densities, charge transport is dependent on the applied bias, where the carrier density in steady-state is low near short-circuit conditions, but increases towards open-circuit conditions. The electric-field distribution within an operating solar cell is one of the defining characteristics of its operational mechanism, determining which regions are dominated by carrier drift or diffusion under given biasing conditions. Unintentional defects in the bulk or at device interfaces can affect the electric field inside the device. When the localized states are deep-lying energy levels within the band-gap, they can pin the Fermi level in the bulk of the intrinsic layer or at the interfaces, limiting the control over the electric field distribution [83]. In particular, the Fermi-level pinning can impose a limitation on V_{OC}, where the filling of sub-bandgap states under illumination limits the quasi-Fermi level splitting.

In conclusion, as mentioned above, a deep understanding of the defect zoology, its nature, the related energy activation levels, and their behaviour in a working device is of paramount importance to achieve high conversion efficiencies. One of the key steps in the realization of light-harvester systems based on perovskites is the development of reproducible synthetic protocols that enables the control over the defect chemistry.

Chapter 2

Materials and Methods

In this chapter we will describe the experimental details of the research. We will discuss the sample fabrication processes and the specification of materials employed. Subsequently, we will present the commercial set-up used for the characterization.

2.1 Device and sample fabrication

2.1.1 Chemicals

Since has been proven (citation CHen) that the material used to synthesize the perovskite materials have an impact on the morphology and optoelectronic properties of the semiconductor, here is the list of the materials employed. All chemicals were used without any further purification.

Sigma Aldrich (Mercks): Lead(II) bromide ($PbBr_2$, 99.999% trace metals basis), cesium carbonate (Cs_2CO_3, reagentPlus, 99%), methylamine (33 wt.% in ethanol, $\geq$98%) butylamine (BuAm, 99.5%), iso-propanol (IPA, anhydrous, 99.5%), Acetone, Chlorobenzene (CB), Diethyl ether (DE, anhydrous, $\geq$99.7%), Hydroiodic acid (HI, 57wt.% in H_2O, with stabilizer), Toluene (TOL, anhydrous, 99.8%) propionic acid (PrAc, 99.5%), n-hexane (HEX 99.5%), titanium(IV) iso-propoxide (99.999%), 4-tert-butylpyridine (tBP), and lithium bis(trifluoromethylsulfonyl)imide (Li-TFSI).

DyeSol: Methylammonium iodide (MAI), methylammonium bromide (MABr), formamidinium iodide (FAI).

Lumtec: 2,2',7,7'-tetrakis(N,N-di-p-methoxyphenylamine)-9,9-spirobifluorene (spiro-MeOTAD).

Concentration of MAI (mM)	Temperature (°C)	d (nm)
63	25	≤ 200
45	25	≈ 250
63	70	≈ 300
63	90	≈ 450
31	25	≈ 750
45	70	≈ 2000
45	90	≈ 4000
31	70	≈ 5000
31	90	≥ 5000

Table 2.1: Two-step deposition details regarding concentration of MAI (reported in mM) and temperature of the isopropanol solution and relative average crystallite size dimensions (d), obtained from SEM images (Fig. 3.2 in Chapter 3).

2.1.2 Methylammonium lead halide perovskites

Precursor synthesis

For the preparation of $MAPbI_3$, a home-made organic precursor was employed. The synthesis of MAI salt follows a well established procedure. Methylamine (MA) solution reacted with HI, in presence of Ethanol (EtOH) at 0°C. The reaction is lead in excess of methylamine. Typical quantity employed are: 48 ml of MA solution, 20 ml of HI and 200 ml of EtOH. After two hours under continuous stirring, the solution was dried using a rotary evaporator, obtaining a white-colored powder. To increase the purity of MAI salt, the product was washed at least two times in EtOH and DE, and subsequently dried in a vacuum oven for 24 hours.

Thin film deposition

The $MAPbI_3$ perovskite samples were deposited following the *two-step deposition* process, under nitrogen atmosphere.

Soda-lime glass. The substrate is cleaned by an ultra-sonication bath in acetone and IPA for 10 minutes each, and treated with oxygen plasma for 10 minutes before the use. The clean glass is then heated on a hotplate at 70°C. The PbI_2 precursor, dissolved in DMF (1 M, i.e. 462 mg/ml) is warmed up at 70°C and spin-coated at 2000 r.p.m. for 60 s, obtaining a uniform layer, with a thickness of 300 nm. A subsequent annealing at 70°C for 30 min was required in order to obtain the PbI_2 thin film. The conversion to perovskite happens when the substrate is dipped in a MAI solution in IPA. After 2 minutes, the sample is finally rinsed in anhydrous IPA, to remove the non-reacted components. The details about the effect

of different concentration and different temperatures of the MAI bath are presented in details in Table 2.1.

Meso-porous Al_2O_3. A commercial alumina nanoparticles dispersion (20 wt.% in IPA, purchased from Sigma Aldrich) was spin-coated at 2000 r.p.m. to form a $1\mu m$ thick meso-porous layer, dried at 150°C for 45 min. The $MAPbI_3$ perovskite was deposited as explained in the previous paragraph. The $MAPbBr_3$ solution (5 wt.% in DMF, equimolar ratio for MABr to $PbBr_2$) was spin-coated at 3000 r.p.m. and immediately heated on an hotplate at 100°C for 15 min.

2.1.3 Cesium lead bromide perovskite nanocrystal inks

The synthesis requires 2 ml of HEX, 1 ml IPA, and 5 μl of Cs precursor solution. This is prepared as following: 2 M of Cs_2CO_3 in PrAc, with the cesium salt dissolved in pure PrAc at room temperature. Quickly after, 100 μl of $PbBr_2$ precursor solution was injected. This solution contains 0.5 M of inorganic salt dissolved in a mixture of PrAc, IPA and BuAm (in equal volume ratio). The two solution are mixed in ambient air and at room temperature, under heavy stirring. All the details about the optimization of the concentration of the latter solution and the volume ratio between the solvents are present in the Chapter 4. The reaction is completed in 10 seconds, turning bright green, which indicates the successful crystallization. $CsPbBr_3$ nanocrystals are then centrifuged for 2 min at 1000 r.p.m. and re-dispersed in the desired amount of the solvent chosen for the thin film deposition.

2.1.4 Device fabrication

To realize the so-called «standard architecture» device the following steps are followed. Fluorine doped Tin Oxide (FTO)-coated glass sheets (2.5 x 2.5 cm^2) are etched with zinc powder and HCl (2 M, diluted with distilled water) to obtain the required electrode pattern. The substrates are cleaned in a ultrasonic bath in a sequence of Alconox detergent (2% v/v in distilled water), distilled water (two times), IPA, acetone and IPA again for 10 min, respectively. The substrates are then blown dry with a N_2 gun and finally treated with oxygen plasma to remove the last traces of organic residues. For the electron-extracting material, a compact layer of titanium oxide (TiO_2) is deposited as following: the TiO_2 precursor solution is filtered with a 0.22μm PTFE filter, and then spin-coated at 2000 r.p.m. for 40 s. The substrates are sintered at 500°C for 45 min. The precursor solution is prepared by mixing 6 μl of HCl (2 M in distilled water) in 1 ml of anhydrous IPA, with a titanium iso-propoxide solution (Ti-iso) in anhydrous IPA (140 μl Ti-iso in 1 ml of IPA). Once the substrates are cooled down, the perovskite-based active layer can be deposited on top, by spin-coating or bar-coating techniques. The

samples are then transferred into a N_2-filled glove box for the deposition of spiro-MeOTAD as the hole-transporting material (HTM). The HTM is spin-coated at 1000 r.p.m. for 45 s. The HTM solution employed is prepared by dissolving 75 mg of spiro-MeOTAD, 32 μl tBP, and 18.8 μl of a stock solution of 520 mg/ml Li-TFSI in acetonitrile in 1 ml anhydrous CB. After 12 h of exposure to dry air, a 75-nm-thick gold film is thermally evaporated at pressure below 1x10^{-6}.The total area obtained for the devices was 0.0935 cm^2.

2.2 Sample characterization techniques

Absorption

All the absorption measurements have been performed with a Perkin Elmer Lambda 1050 spectrophotometer. In order to evaluate the Optical Density (OD) of the samples in an accurate way, a special module of the spectrophotometer with an integrating sphere has been selected. This allowed the collection of both the total reflectance (R%) and the total transmittance (T%) of the samples. According to Lambert-Beer's law:

$$I_T = (I_0 - I_R)10^{-OD \cdot d}$$

where I_T, I_0 and I_R are, respectively, the intensity of the transmitted, incident and reflected light, while d represent the material thickness. To evaluate the value of d, a cross-section SEM image is acquired.

Photoluminescence

The continuous-wave excitation photoluminescence measurements (PL) were performed with a spectro-fluorimeter (Horiba JobinYvon). A 450 W Xenon short-arc lamp coupled with two single-grating excitation and emission monochromators is used to excite the sample. The emission spectra were collected using a VIS Si-based (400–800 nm) solid-state photo-diode. On the collection line, a long pass filter was used in order to filter the excitation light.

Time Resolved Fluorescence

Time-resolved photoluminescence measurements are performed qith a femtosecond laser source and a streak camera as detection system (Hamamatsu C5680). An unamplified Ti:Sapphire laser (Coherent Chameleon Ultra II) with an operational frequency of 80 MHz is tuned to obtain pulses at 700 nm, energies of $\approx$50 nJ, and temporal bandwidth of $\approx$140 fs and and spectral bandwidth $\approx$5 nm, respectively. The emitted fluorescence is collected and

filtered with a long-pass filter chosen accordingly to the emission range (to remove the excitation light). The light is then focused on a spectrometer of the detection system.

Scanning Electron Microscopy

All the images have been collected using a commercial Jeol 6010-LV, working in high vacuum with a tungsten filament keeped at bias of 20 kV.

X-Ray Diffraction

The X-ray diffraction spectra are recorded with a diffractometer (Bruker D8 Advance) equipped with Bragg-Brentano geometry. The X-Ray emission is obtained with a Cu Kα_1 (λ = 1.544060 Å) anode at operating voltage of 40 kV and operating current of 40 mA. All the diffraction patterns were recorded at room temperature over an angular range (2θ) between 10° and 60°, a step size of 0.020° and an acquisition time of 2 s.

2.3 Devices performance investigation

Current density–Voltage measurements set-up

The current density-voltage (J–V) characteristics have been measured with a computer-controlled Keithley 2400 SourceMeter. The simulated Air Mass 1.5 Global (AM 1.5G) irradiance was provided by a Class AAA Newport solar simulator. The light intensity was calibrated with a silicon reference cell with a spectral mismatch factor of 0.99. The specific parameters such as scan rate, scan direction and pre-treatment are reported for each measurement along with the J–V curve. All the devices have been measured in air, without any device encapsulation.

Chapter 3

Role of micro-structure in the opto-electronic properties of hybrid lead halide perovskites

This chapter is dedicated to the accurate analysis of the effects of the synthesis' environmental conditions over the final morphology of perovskite self-assembled crystals. The related optical properties of perovskites are then investigated, retrieving a strong correlation between the two. The guideline is represented by the need of progressive insights on the optical properties of the semiconductor. Starting from concepts embedded in the devices, up to a general comprehension of the properties of the material, with the purpose of focusing the problems that affect the realization of highly efficient solar cells.

Lead-halide perovskite thin films present a wide range of morphologies, depending on the processing method, with average grain size varying from tens to thousands of nanometers. It has been shown that the final device performances, as well as the absorption and the photoluminescence properties together, are heavily affected by the obtained crystalline morphology. This knowledge is a cornerstone of the research in the field, and it has been built in the last few years with a joint effort of the community. The aim of the initial work was, back in 2014, trying to build a reliable and reproducible protocol for the deposition of the material, as some fundamental questions were still to be addressed. In this context, a variety of behaviours were observed: different selective materials are embodied into solar cell architectures as charge-selective contacts, and perovskite materials must be directly crystallized on them. Various chemical compositions, surface energies and morphologies were affecting the photo-physical response of the semiconductor, producing a plethora of responses, sometimes unwanted. Building a coherent and comprehensive vision of the subject was, then, urgently crucial.

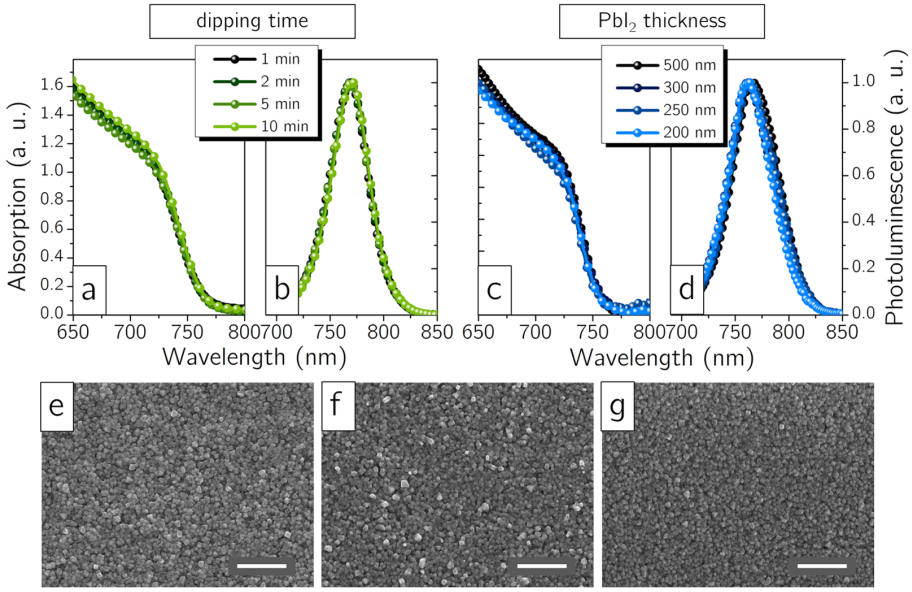

Figure 3.1: On top left, a) absorption and b) PL spectra of $MAPbI_3$ deposited on glass, by a two-step deposition method. Varying the dipping time of the PbI_2 thin film (fixed thickness at 300 nm) into the organic solution (fixed concentration at 0.063 M). From black to bright green, the dipping time is varied from 1 minute to 10 minutes. On top right, c) absorption and d) PL of $MAPbI_3$ obtained with a variation on the initial PbI_2 layer thickness (fixed concentration at 0.063 M, dipping time at 2 minutes). From black to bright blue, the PbI_2 thickness is varied from 200 nm to 500 nm. In both experiments, the temperature of the MAI bath is fixed at 25°C. As a result, no influence on the basic optical properties is observable. On the bottom, top-view SEM images of the samples investigated: e) dip time of 2 minutes with PbI_2 thickness of 300 nm; f) dip time of 10 minutes with PbI_2 thickness of 300 nm; g) dip time of 2 minutes with PbI_2 thickness of 500 nm. As a guide for the eye, in the images, scale bars of 1 μm are reported.

3.1 How to control the average crystallite size

To shed light on the growth mechanism of the hybrid methylammonium lead iodide perovskite ($MAPbI_3$), the choice of the deposition method is of paramount importance. The final aim is to gain a fine control over the obtained mean crystal dimensions, in order to systematically probe the basic optical behaviour of the material in each condition. In this sense, the simplest sample architecture is chosen: the semiconductor is grown on a clean and inert glass slide, with a two-step deposition method. This represent the best choice, since it is possible to control independently the greatest number of environmental parameters active in the synthesis process. In fact, the perovskite material is obtained by sequentially expose the inorganic PbI_2 thin film to the organic MAI, which is dissolved in isopropanol (IPA). This process allows the variation over PbI_2 thickness and, only in a second time, the condition over the MAI exposure (i.e. reaction time, concentration of the organic moiety and temperature of the environment during the reaction).

In Fig. 3.1, on top, are reported the absorption and photoluminescence spectra of $MAPbI_3$ samples obtained by varying the dipping time of the PbI_2 thin film into the organic solution. The value of PbI_2 film thickness, the concentration of the MAI solution and the temperature of the bath are kept fixed at 300 nm, 0.063 M and 25°C, respectively. In the same figure, on the bottom, is reported the results of the PbI_2-thickness-variation experiment. If the PbI_2 solution (1 M in DMF) is deposited by spin coating at different spin speed, the final thickness will vary accordingly. Going from spin speed of 1000 r.p.m. to 6000 r.p.m., the thickness is reduced from 500 nm to 200 nm. After the evaporation of the solvent and the crystallization of the PbI_2 film, these samples are dipped into the room-temperature MAI solution for the same time (2 minutes) and at a fixed MAI concentration (0.063 M). It is clear that none of the two parameters have a role in the determination of the optical characteristics of the final material. As a cross-check, the morphology of the so-obtained perovskite films are investigated by *secondary electron microscopy* (SEM), as shown in Fig. 3.1, bottom panel.

Conversely, it is possible to observe a growth in the mean crystallite dimension (d) when the temperature of the bath is increased, or when the concentration of the organic molecule is reduced, as reported the first two panels in Fig. 3.2. Here, the SEM images of a series of $MAPbI_3$ thin films are reported, in which the samples are named with the corrispondent synthesis procedure (M = millimolar concentration of MAI used, T = temperature of the solution). Subsequently, a set of perovskite thin film is realized varying simultaneously temperature and concentration. A combined action of the two parameters (i.e. decreased concentration and increased temperature) allows the crystallization of macro-domains up to 20 times bigger than the starting ones. Specifically, it is possible to go from $d = 200$ nm (M63T25) to $d \geq 5000$ nm (M31T90). In Fig. 3.3 are reported the optical characteristics of this last set of samples. It has to be noticed, first of all, that the optical band-gap undergoes a continuous red-shift towards longer wavelengths, as the value d increases. At the same time, the shape of the absorption spectra changes, with an excitonic-like feature superimposed to the step-function-like absorption which becomes clearer as d decreases. Interestingly, the effect of the micro-structure on the optical behaviour of these hybrid materials is not limited to the absorption features. In the right panel of Fig. 3.3 it is clearly visible a dependence of the photoluminescence (PL) emission peak from the value d. Specifically, as d increases, a red-shift of the maximum emission wavelength is registered.

The possibility to finely tune the perovskite average crystallite size offers the chance to uniquely prove that the optical behaviour of the semiconductor is deeply interconnected with the morphology. The observed shrinkage of the optical band-gap in larger crystallites can be explained if a stress-induced tilting of the I-Pb-I bond angle is considered. In fact, previous reports investigating 2D-perovskite materials had shown a possible tuning of

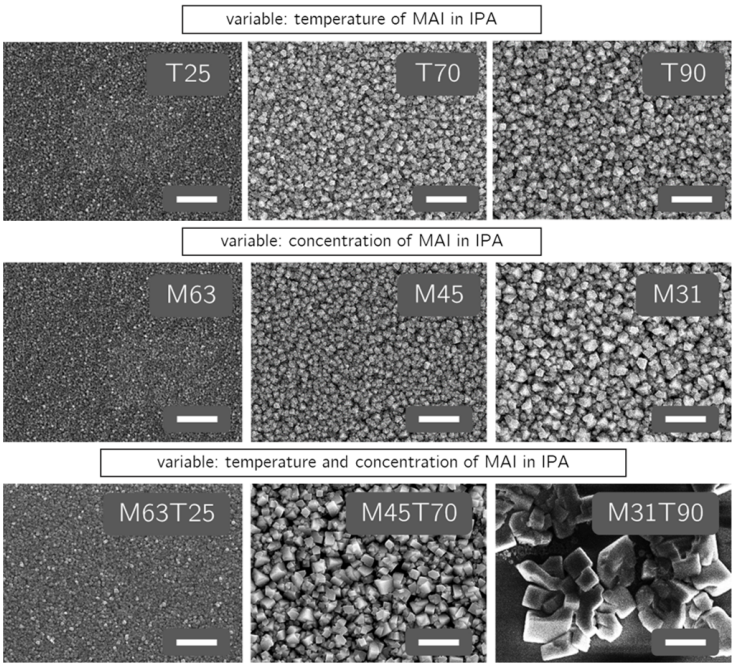

Figure 3.2: SEM images of $MAPbI_3$, showing different average crystallite size. The samples are named with the corrispondent synthesis procedure (M = millimolar concentration of MAI used, T = temperature of the solution). On top, variation over the bath temperature, changed from 25°C to 90°C. In this case, the concentration of MAI in IPA is kept fixed at 0.063M, as the PbI_2 film thickness (300 nm) and the dipping time (2 minutes). In the middle, variation over the molar concentration of MAI, decreased from 0.063 M to 0.031 M, while the temperature is kept at 25°C, with a PbI_2 thickness of 300 nm and a dipping time of 2 minutes. On the bottom, simultaneous variation over temperature and concentration of MAI in IPA, while the PbI_2 film thickness (300 nm) and the dipping time (2 minutes) are identical for all the samples. As a reference, scale bars are 1μm.

the halide-metal-halide bonding angle exploiting a different degree of relaxation in the arrangement of the organic moieties [86]. This suggests that the same effect could play a role even in the 3D counterparts. More recently, as a matter of fact, some theoretical studies had simulated the behaviour of the optical band-gap of $MAPbI_3$ when the I-Pb-I bond is distorted, predicting a variation over 1 eV of the latter [18], [28]. In the case considered here, the larger the crystal is grown, the lower is the stress accumulated in the lattice over the Pb-I bond angle, inducing a red-shift in the absorption onset. To demonstrate the last point, a more detailed investigation has been carried out, as discussed in the next section.

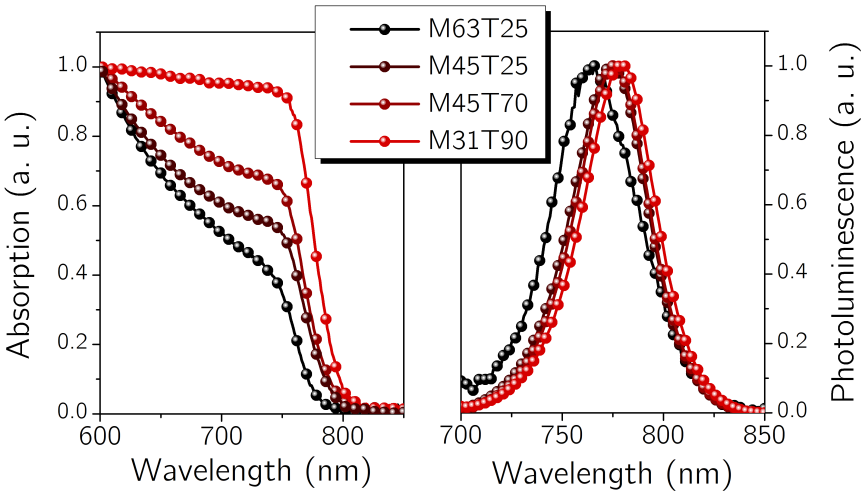

Figure 3.3: Absorption and photoluminescence spectra of $MAPbI_3$ on glass, with different average crystallite size (d). Specifically, M63T25 ($d = 200$ nm), M45T25 ($d = 500$ nm), M45T70 ($d = 1000$ nm), M31T90 ($d = 5000$ nm).

3.2 The role of the orientational order of the organic cation

To investigate more deeply the correlation between morphology and optoelectronic behaviour, a $MAPbI_3$ film is fabricated by two-step deposition on a 3-μm-thick alumina meso-porous scaffold (meso-Al_2O_3, details about the preparation of the samples are reported in Chapter 2). This configuration provides simultaneous access to two distinctive structural morphologies: the crystalline phase grown within the scaffold («meso-phase») which, on average, limits the crystal size below 50 nm, and a thick capping layer on top of the scaffold, consisting of crystals up to hundreds of nanometers (> 500 nm). Varying the pore sizes of the meso-Al_2O_3, it is possible to confine the growth of the semiconductor to specific ranges. This allows to optically probe selectively different crystalline dimensions in a reproducible way. In Fig. 3.4, in the left panel, are presented the UV-Visible absorption spectra collected at 4.2 K of $MAPbI_3$ samples of three different d ranges. Notably, the spectrum given by the largest crystals ($d \geq 500$ nm, red curve) shows the expected red-shift, but also a strong excitonic feature which, conversely, is undetected in the same material grown in the meso-porous scaffold ($d \leq 50$ nm, blue curve).

Lead-halide materials show exciton binding energies of different values, going from 2 up to 50 meV. Initially it was ascribed to the use of various techniques employed to assess the value, while it has been shown that the major cause for the discrepancy arise from the local micro-structure and its variability from sample to sample. The exciton stability depending on the

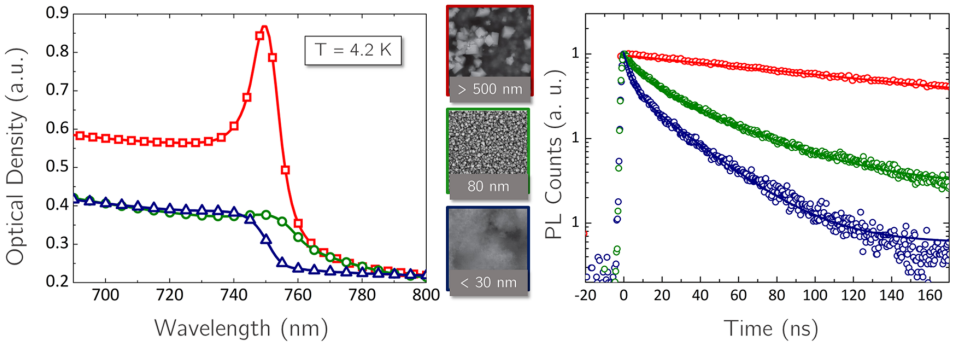

Figure 3.4: UV-Visible absorption spectra of $MAPbI_3$ samples acquired at 4.2 K. The samples are deposited on glass, with different d values. $d \geq 500$ nm, red curve, $d \approx 80$ nm, green curve and $d \leq 30$ nm, blue curve. On the right, photoluminescence dynamics the same samples. Both measurements have been performed by Dr. V. D'Innocenzo. In the center, SEM images of the samples measured.

value d has been intensively studied [89]. Dr. G. Grancini and Dr. A. R. S. Kandada showed that the strong contribution of various phonon modes to the electron-hole screening, with the variation of the degree of order/disorder of the organic ion over different film architectures, can result in tuning of the exciton binding energies. In short terms, the degree of polycrystallinity, i.e. the mean crystallite size or the surface-to-volume ratio in perovskite thin films, induces electrostatic potential variations that can suppress the exciton formation or its stabilization. So, in polycrystalline environment the orientational order of the organic cation is playing a crucial role. To better explain this, it has to be considered that the organic cation possess a permanent dipole moment, which generates an electrostatic potential gradient that has an influence on the electron–hole separation. Thus, the orientation of a single organic molecule is influencing the orientation of the nearest molecules in the lattice. The freedom in rotation of the organic part generates a dielectric response. Raman analysis on the meso-phase of $MAPbI_3$ suggests that dipoles in smaller crystals might be more randomly oriented in the inorganic cage [87], [88]. Thus, it has to be expected larger perovskite crystals to show more extended region of cooperatively ordered organic molecules. In addition, to see the microscopic effects of molecular disorder, a simulation of polycrystalline thin films has been elaborated by collaborators (Dr. J. M. Frost and Dr. A. Walsh, University of Bath), in which the variation of electrostatic potential is studied as a function of the polycrystalline degree [89]. The grain boundaries are induced by incorporating inactive lattice sites (point defects) in the simulation (at different densities, 6% and 10%). The standard deviation in the electrostatic potential is evaluated against the temperature and degree of polycrystallinity. Disorder grows with temperature in both systems, as would be expected from statistical mechanics, generating increasing electrostatic potential variance. Interestingly, the largest variation

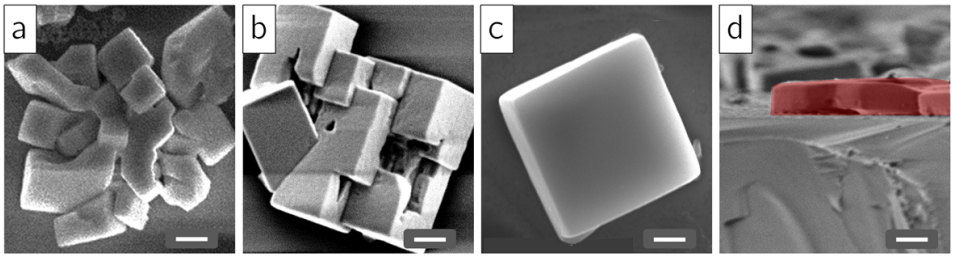

Figure 3.5: SEM images of three $MAPbI_3$ samples obtained by the two-step M31T90 recipe, with progressively thinner starting PbI_2 layer thickness (scale bars of 2 μm. a) PbI_2 = 300 nm; b) PbI_2 = 200 nm; c) PbI_2 = 100 nm; d) cross-section image of c) with scale bar of 1 μm, in which the perovskite material has been highlighted in red.

occurs at grain boundaries, where the dipole twinning is disrupted. These simulations confirm that the local screening can be controlled by the local order within the crystal. With larger, less defective crystals (i.e. less boundaries) the local screening is minimized. Thus, electron–hole separation due to electrostatic disorder should be significant in small crystals, countering the Coulomb attraction that exists between electrons and holes, but weaker in large crystals, allowing for Wannier-Mott-type exciton formation. It is evident that a sensitivity of the molecular order to crystal quality, defects, as well as induced strain and device history exists. It implies that the material processing plays a crucial role in the determination of the nature and dynamics of the photo-physical species and mechanisms characterizing each hybrid perovskite-based sample.

3.3 Local probing of perovskite optical response

Despite the demonstration of the two regimes, it is not clear yet over which spatial length scale the crystal coherence affects the photo-physical properties of the semiconductor. To address this question, the ultimate case study should be a single-crystal sample. However, a single crystal shows energetic dishomogeneities for the optical band-gap between surface and bulk, which follows the same trend as the small and large crystallites. This is easily explained taking into consideration that every surface of a crystal is an extended defect, and it should be considered comparable to the sample made by small crystallites. Moreover, due to the extremely high absorbance of a single crystal, the absorption spectra presented in the literature have been measured through reflectivity, which is way more sensitive to the surface than to the bulk, giving spectra that do not show any excitonic feature. But, at the same time, the *external quantum efficiency* (EQE) spectra of solar cells embodying a single crystal, which are more sensitive to the bulk than to the surface, show a defined exciton feature at the band-edge, in contrast to polycrystalline film-based devices [91]. To overcome the high-absorption

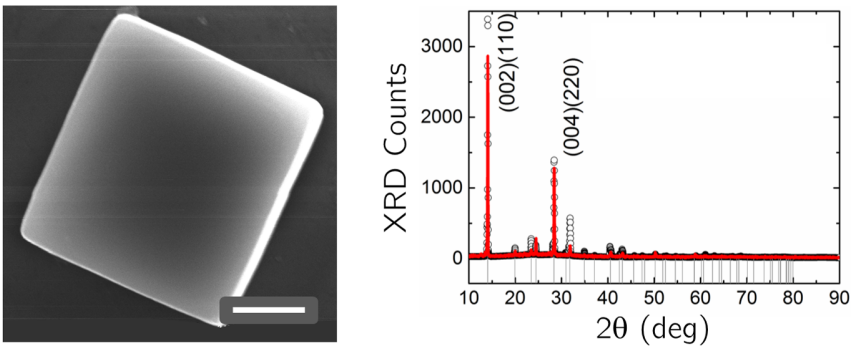

Figure 3.6: On the left, top-view SEM image of the crystal investigated (scale bar 2 μm). On the right, XRD spectrum of the sample, (experimental data are dots, fitting in red). The refined unit cell parameters employed are: $a = 8.699$ Å, $b = 8.699$ Å, and $c = 12.421$ Å. The XRD analysis has been performed by Dr. C. Giannini (Institute of Crystallography, CNR, Bari).

issues, platelets of $MAPbI_3$ are synthetized, which, thanks to their moderate absorbance, allows to directly map the photo-carriers dynamics. This is done with sub-micrometer spatial resolution by a combination of space- and time-resolved optical spectroscopy. The samples investigated have been obtained by a further optimized version of the two-step procedure explained in the first part on the Chapter. The top-view of the crystals are reported in Fig. 3.5. In this case, a progressively thinner PbI_2 layer is dipped in the same hot solution of diluted MAI (0.031 M at 90°C). Going from a PbI_2 thickness of 300 to 100 nm the crystals grow in a progressively ordered way. These micro-crystals possess a large aspect-ratio, as showed in Fig. 3.5, d).

Fig. 3.6, on the left, shows top-view SEM image of the crystal investigated. To assess the structural phase and the degree of crystallinity, or the coherence-domain size of the sample, the XRD spectrum is required, and it is shown in Fig. 3.6, on the right. Sharp diffraction peaks, indexed as the tetragonal $MAPbI_3$ structure, denote not only a high level of crystallinity and a high degree of orientational order in the growth of the crystals. Fitting of the profile (reported in red in the Figure) retrieves a coherence length larger than 330 nm. It has to be noticed that this estimation is instrument resolution-limited, and it indicates that the micrometer-large perovskite crystals are made of mono-crystalline regions extending, at least, over 330 nm. As reported in Fig. 3.7, a), the same crystal grown on a clean glass is investigated through an optical probe, giving a transmission image. The absorption at 680 nm is homogeneous across the crystal, indicative of a smooth surface with uniform thickness. For probing the photo-physics on different spots within the crystal itself, this is of high importance, because it ensures homogeneous excitation density. At the boundaries of the single platelet, a higher degree of structural disorder is expected, which induces a local modulation of the semiconductor optoelectronic properties, and a shift in the band-gap

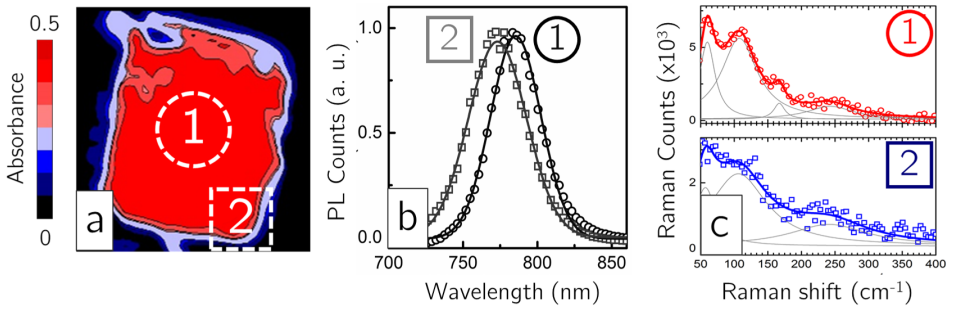

Figure 3.7: a) linear absorption image with a probe wavelegth of 680 nm. Marked, two characteristic regions that are analyzed; b) normalized PL spectra obtained by using the microscope exciting at 460 nm in region 1 and 2, reporting a spectral shift of 10 nm; c) micro-Raman spectra at region 1 (on top, in red) and 2 (on the bottom, in blue) of the platelet (excitation at 532 nm). The measurements have been performed by Dr. G. Grancini (Center for NanoScience and Technology, IIT at Politecnico di Milano) and D. Viola (Politecnico di Milano).

is observed (Fig. 3.7, b). To gain a comprehensive picture of the structural properties of the sample, the lattice vibrations have been characterized too. The Raman spectra have been measured in two characteristic regions of the crystal, marked in Fig. 3.7, a): region 1, closer to the center of the sample, and region 2, closer to the border. The main features of the Raman spectra (Fig. 3.7, c) match with those reported in literature for this type of material. However, first of all, one can notice a greater sharpness of the vibronic bands in region 1, which is generally a signature of higher structural order. This comes along with the presence of a defined peak at 160 cm^{-1}, assigned to libration of the MA cation [88]. This feature is expected to be sharper when the organic cation has a reduced degree of freedom within the crystal unit. This is observed by reducing temperature, or in a more ordered crystalline lattice, that is verified when the MA cations fix their position in the preferential «head-to-tail» geometry. The presence of this marker proves that the degree of freedom of the organic moiety is the switcher able to induce, through hydrogen-bonding interactions, the local distortion of the lattice. This modifies the local dielectric response, with the final effect of tuning the optoelectronic properties of the material. In region 1, the cations have a reduced degree of freedom within the crystal unit, resulting in a lower lattice strain, and thus in a lower band-gap. To further investigate the sample, the spatially resolved photo-induced dynamics (ultrafast TA microscopy) have been measured. With respect to standard ultrafast TA spectroscopy, which interrogates volumes of tens to hundreds of micrometers, TA microscopy and its sub-micron spatial resolution, is able to resolve spatial dishomogeneities in the photo-physical response of the sample. The TA microscopy experiments indicate that the electron-hole correlation is higher in region 1, with reduced local dielectric constant, with respect to region 2. Thus, the com-

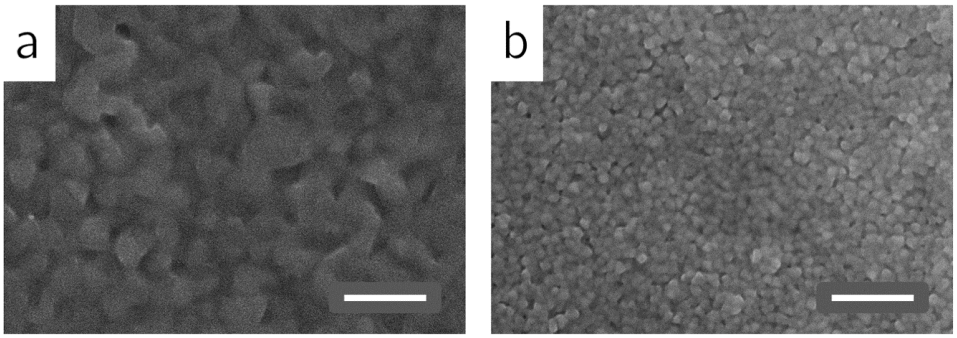

Figure 3.8: Two examples of $MAPbI_3$ polycrystalline thin film for photovoltaic applications, obtained by SEM. The active material is assembled onto a) inorganic electron-extraction layer (titanium oxide, accordingly to [110]) and b) onto polymeric hole-selective contact (PEDOT:PSS, as reported in [92]). Both deposition techniques and environmental parameters have been optimized independently. Scale bars represent 1 μm.

bination of Raman microscopy with TA microscopy has provided evidence that an enhanced structural disorder, when moving from the center to the border of the crystal, is responsible for an increase in the band-gap.

In light of the reported results, it is possible to conclude that the observed changes in the characteristic absorption and emission features are related to the local conformation of the crystalline lattice. The distortion of the halide-metal bonding angle, thus the inorganic cage status is affecting the overall electronic band structure, in which a shift towards longer wavelengths of the band-edge is created when the distortion increases. The steric hindrance and the local cooperative motion of the organic cations are affecting the ground state crystalline band structure, influencing the screening of the photo-generated charges. This effect can provide both free-carrier and excitonic regimes for a single chemical composition of the semiconductor, with a dependence on the extension of the crystalline coherence regions.

3.4 Perovskite in a real photovoltaic device

As mentioned at the beginning of the Chapter, the urgency of addressing fundamental questions regarding the nature of photo-excited species and the ability to foreseen opto-electronic responses, while controlling synthetic parameters, were motivating the studies just presented. However, in a real technological application, perovskite must assemble onto specific materials that are different from bare soda-lime glass slides. Thus, optimizing the photon-to-electron conversion performances of a photovoltaic device will require additional work, to assess the characteristics of contingently selected solar cell architectures. Of course, there are few fundamental characteristics that the active layer must, *a priori*, fulfil: the first ones are full coverage of the substrate and reasonable roughness. Any pinholes in the vertical

direction would create shunting pathways for the photo-generated charges, decreasing the overall performance of the devices. At the same time, perovskite layers with 100% coverage but highly rough would still suffer from not-optimal charge extraction, favouring the rise of hysteretic behaviours. Specifically, in order to prevent direct contact between perovskite and the evaporated metal, the thickness of the charge-selective interlayer must be increased. The second characteristic is the correct optical thickness. The absorber layer in a photovoltaic device must maximize light absorption, i.e. be thick enough, but simultaneously efficient in the charge collection, i.e. thin enough to prevent charge recombination, a parameter that will be influenced by the amount of non-radiative recombination centers present in the semiconductor. The optimization of the perovskite deposition protocols, moreover, must meet the requirements imposed by the choice of the charge-extraction layers. Some advancements, in this contest, have been achieved in parallel to the results here reported, simultaneously with several other contributors from the scientific community. These works have been conducted in the same research group, with a contribution of the author [92], [110]. From the latter and the just-exposed results, the existence of a tight tolerance window for the optimal processing parameters of these self-assembled materials emerges. A novel approach is now proposed: the realization of a perovskite active layer by the deposition of an ink composed by suspended nanoparticles. The specific formulation of the ink can be tailored to guarantee the film formation and the best opto-electronic properties needed. In this case, the simultaneous optimization of large-area uniform coverage with a high-quality crystal growth is no longer needed. The results obtained by following this approach will presented in the next Chapter.

Chapter 4

Strongly emissive perovskite nanocrystal inks for high-voltage solar cells

In this chapter, a novel approach for the realization of stable and reproducible perovskite materials is reported. The synthesis of high-quality colloidal perovskite nanocrystals is presented, with an extended investigation over the optimal conditions required to produce the best photon-to-electrical energy conversion. The role of many parameters is considered, showing their role in the crystallization process of the perovskite self-assembly.

4.1 A novel perovskite nanocrystals synthesis

In literature, two different strategies to obtain high-quality and mono-dispersed nanoparticle solutions have been developed. A first one has been presented in 2015 by Protesescu et al. [93], known as the *hot injection* method. In this case a mono-disperse suspension of $CsPbX_3$ nanocrystals (NCs) with cubic shape is obtained by a controlled arrested precipitation of Cs^+ , Pb^{2+}, and X^- ions. The synthesis requires the reaction of Cs-oleate with a Pb(II)-halide precursors in a high boiling solvent (octadecene) at high temperatures ($140 - 200$ °C). The reaction is extremely fast, and after few seconds the perovskite colloidal suspension is obtained. The $CsPbX_3$ size control can be achieved through the management of the reaction temperature, and it is possible to tune the particle dimension between 4 and 15 nm. A mixture of oleyl-amine and oleic acid are added into octadecene to solubilize the lead precursor salt and to colloidally stabilize the nanocrystals. A second strategy has been presented shortly after by Zhang et al. [94], which has been called ligand-assisted re-precipitation, or LARP. The method relies on the re-precipitation through solvent mixing, which is a simple technique employed in the preparation of organic nanoparticles or polymer dots [95], [96].

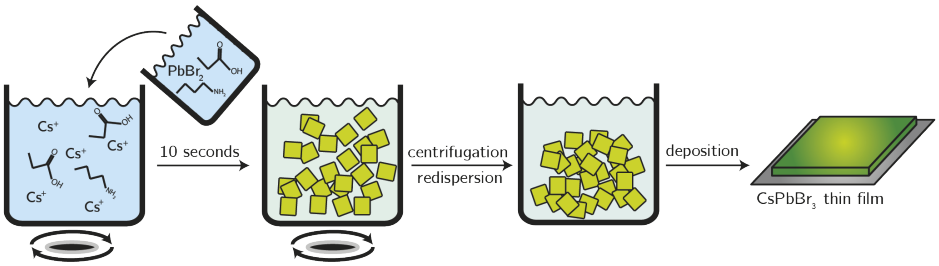

Figure 4.1: Schematic representation of the NCs synthesis. In this, the $PbBr_2$ precursor solution is injected in a hexane/isopropanol mixture containing Cs^+ cations, under heavy stirring. After a mild centrifugation and the redispersion in the desired solvent, the ink can be used for deposition of thin films.

The synthesis is accomplished by simply mixing a solution of CH_3NH_3Br and $PbBr_2$ in DMF into a vigorously stirred anti-solvent (toluene, hexane and similar). Adding long organic chains, the controlled crystallization of precursors into colloidal nanoparticles is achieved. Without using long-chain lignds, the LARP method gives micrometer-sized particles with very low PLQYs (<0.1%). By incorporating n-octylamine and oleic acid as ligands into the reprecipitation process, it is possible to produce luminescent dots with absolute PLQYs over 70%. Although it is possible to finely control the size distribution of the NCs and their luminescence efficiency, the two methods show several limitations. First, both syntheses require degassing for the precursors as initial step. The solvents employed are toxic and possess extremely high boiling points (octadecene $T_{eb} = 315°C$, DMF $T_{eb} = 153°C$, DMSO $T_{eb} = 189°C$), therefore are less amenable to scale-up in industrial processes. It is worth to highlight as well that solvents like DMF, other than extremely toxic and harmful, are not neutralized by the glove-boxes filters. As a matter of fact, they tend to accumulate in the atmosphere, affecting the surface properties of the substrates and consequently the perovskite crystal properties [97], [98]. Moreover, the choice of ligands was limiting the application of NCs to down-converter materials [94]. In fact, once the NCs have been deposited in a thin film, the long alkyl chains form an insulating layer around the semiconductor, hampering the charge transport in the film and their collection. Only in July 2016, Swarnkar A. et al. demonstrated the first perovskite quantum-dot-based solar cells [109]. However, the process presented in this work still relied on many delicate passages. First, the nanocrystals are synthetized with a modified hot injection method, with the use of long alkyl chains that must be removed while realizing the solar cell. Second, as indicated in the paper, the preparation of the colloidal dots requires several hours, with sequential purifying washing-steps, in which any excess of components removes the surface ligands, causing the NCs to agglomerate and revert to a photo-inactive phase. Moreover, the suspension must be kept in the dark at 4°C for 48 hours, to precipitate the un-reacted

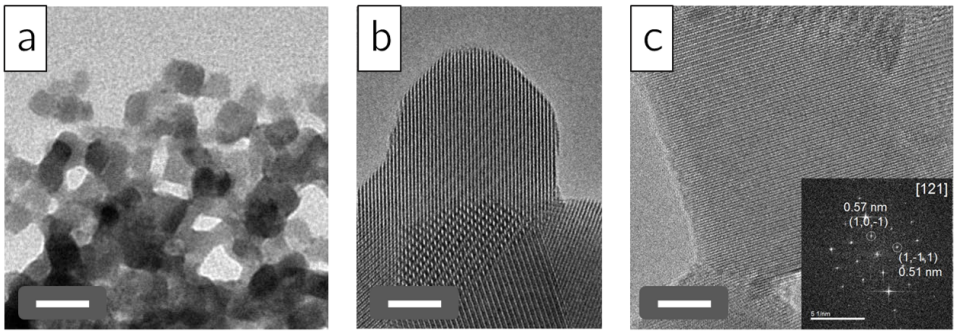

Figure 4.2: a) TEM image of $CsPbBr_3$ drop-casted on a substrate with a scale bar of 50 nm; b) TEM image that shows domain size of $15-20$ nm, with scale bar of 5 nm; c) HR-TEM image of a crystal (scale bar 5 nm), while in the inset diffraction pattern matching the orthorhombic $CsPbBr_3$ phase. The analysis is carried out by Dr. G. Bertoni (IIT, Genova).

precursors, and centrifuged multiple times before the use. Only now the ink is ready to be deposited by sequential deposition cycles: at every step, the thin film must be exposed to a saturated solution of $Pb(Ac)_2$, or $Pb(NO)_3$, to restore the conductivity in the final active layer. While the paper was being published, the work presented here was under revision. The paradigm on which this work was conducted is intrinsically different: the final goal is the realization of a perovskite-based ink in which the ligands can be removed quickly, if not at all.

The synthesis of the $CsPbBr_3$ NC inks has been developed at the Nanochemistry Department of Italian Institute of Technology (IIT) by Q. A. Akkerman of Prof. Liberato Manna's group. As depicted in Fig. 4.1, it is carried out by a simple and fast one-step injection. Cs_2CO_3 salt is dissolved in propionic acid (PrAc), to form a Cs^+ propionate complex. The lead precursor is $PbBr_2$, and it is dissolved in a mixture of isopropanol (IPA), PrAc, and butylamine (BuAm). The dissolution reaction is, in both cases, exothermic, thus no external source of heating is required. As soon as the solutions are injected in the nucleation environment - a mixture of hexane (HEX) and IPA - the crystallization reaction starts, and the nanoparticles form, reaching their maximum size in just few seconds. A simple centrifugation step enables the separation of the so-formed crystals from the reaction agents, followed by a re-dispersion in a clean solvent as final passage. The ink is then ready to be employed for the device preparation. As shown in Fig. 4.2, where the transmission electron microscopy (TEM) investigation is reported, the NCs tended to cluster in large aggregates. This behaviour is not induced by the centrifugation step, since identical aggregates can be observed in samples examined right before washing. These aggregates contain defined crystalline NCs, composed by domains of roughly $15-20$ nm in size. The atomic planes, seen thanks to a high-resolution TEM analysis (HR-TEM, in Fig. 4.2, c),

match those of orthorhombic $CsPbBr_3$. The structural phase of the NCs is then confirmed by the *X-ray diffraction* (XRD) pattern. Further details, acquired by *X-ray photo-electron spectroscopy* (XPS), show that the surface of a drop-casted thin film presents aCs : Pb : Br ratio of 0.90 : 1.00 : 3.00, which is an indication of a slightly Cs-deficient material. It has to be noticed that this technique is very sensitive to the first few nanometers of the film, and this might suggest a surface termination composed by Br-Pb-Br bondings. Thanks to the same measurement set-up, it is possible to determine the carbon content in the film deposited, resulted to be 22 at.%. As reference, a sample of 8.5 nm cubic $CsPbBr_3$ NCs are synthetized. In this case the particles are prepared with the hot-injection technique, with the use of octadecene, oleic acid and oleyl-amine [93]. The latter shows a surface composed of carbon at 88 at.%, a percentage comparable to other reported colloidal NCs synthesized under similar conditions, not necessarily composed by halide perovskites [99]. Thus, the carbon ratio to the overall $CsPbBr_3$ inorganic component shows a 25-fold decrease for this novel synthesis, which is a good starting point to obtain a conductive thin film.

4.2 Emission properties of $CsPbBr_3$ nanocrystals

The growth of the NCs during the synthesis was monitored over time by tracking their PL, which grows as the NCs form and proves that the reaction takes place within the first 10 seconds after the injection of the precursor. The PL and optical absorption spectra have been measured on the purified $CsPbBr_3$ NCs, both for toluene suspensions and for thin film obtained by drop-casting, as reported in Fig. 4.3, a. The NCs in solution had a PL peak centred at 510 nm, with a full-width-half-maximum (FWHM) of 24 nm. In the NC film, the optical absorption edge experiences a red-shifted of about 7 nm, from 515 nm to 522 nm. This may be attributed to a change in the local strain of the NCs surface in the different phase. The PL spectra consistently follow the absorption edges, and retained the same Stokes shift (approximately 10 nm) and FWHM. The photoluminescence properties of the material have been further investigated with a femto-second excitation source, to observe the behaviour under high photon fluxes. The amplified spontaneous emission (ASE) is recorded in a thin film prepared by spin coating (Fig. 4.3, b). The FWHM of the emission is reduced to 4.3 nm, peaking at 522 nm, slightly red-shifted compared to the standard emission. Analysing the ASE intensity versus pump fluence it is possible to determine the ASE threshold for the material, which is a good fingerprint for the optical quality of the semiconductor. Several different NCs batches have been tested, since it is known that the relatively high refractive index of the layer and the film morphology itself could induce optical feedback and modify the ASE threshold value, favouring random lasing. After 62

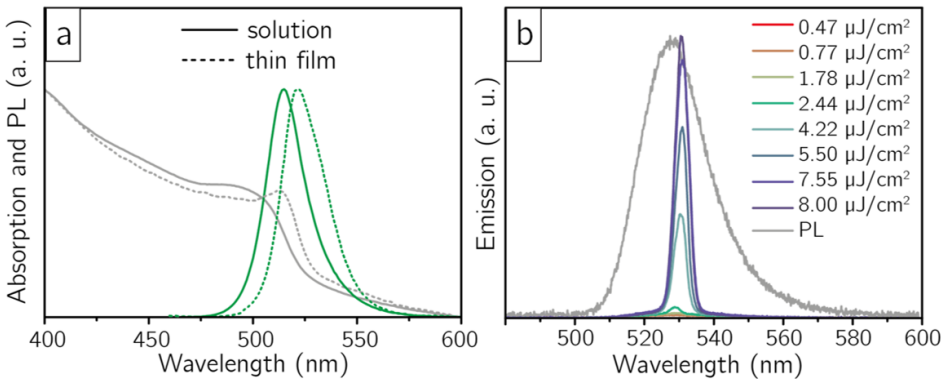

Figure 4.3: a) Absorption and steady-state PL spectra of $CsPbBr_3$ NCs for both toluene solution and spin-coated thin film. A spectral shift of ≈ 10 nm towards longer wavelength is observable. b) Amplified spontaneous emission spectra at increasing pump fluences. Measurements performed by Dr. F. Di Stasio and P. Rastogi (IIT, Genova).

measurement, the value is assess around 2.44 $\mu J/cm^2$, with a minimum of 1.5 $\mu J/cm^2$. It is worth to notice that 1.5 $\mu J/cm^2$ is the lowest value reported for $CsPbBr_3$ NCs and overall for perovskite thin films. This is a strong evidence supporting the high optical quality of the ink, which, even more importantly it is preserved in the related thin films. The value showed here is among the lowest ever reported, even considering other inorganic NCs commonly used in laser devices [100], [101]. A second hint on the quality of the crystals obtained by this novel synthesis comes from the *PL quantum yield* (PLQY), i.e. the percentage of emitted photons respect to the absorbed ones. In a material with a low density of defects the radiative recombination of photo-excited species will be the predominant process following the excitation. Defects, as explained extensively in the Introduction, represent alternative routes to the bi-molecular recombination pathway. Thus, a high PLQY value at low excitation fluences is an indicator of low density of active defects in the lattice. The PLQY value recorded for the ink suspension is about $58 \pm 6\%$, while the thin film shows $35 \pm 4\%$ at excitation fluence of ≈ 250 $\mu W/cm^2$. As a reference, the crystals obtained by hot injection show slightly lower values, $\approx 30\%$. All of the above-mentioned characterizations have been carried out by Dr. F. Di Stasio and P. Rastogi (IIT, Genova).

4.3 High voltage solar cells

Wide-band-gap semiconductors, including halides perovskites as $CsPbBr_3$, can achieve higher open-circuit voltages. Therefore, these materials are of particular interest for applications such as multi-junction solar cells, light-emitting devices with an emission in the visible range, and for solar-powered water splitting applications [102], [107]. Among all the halides perovskite,

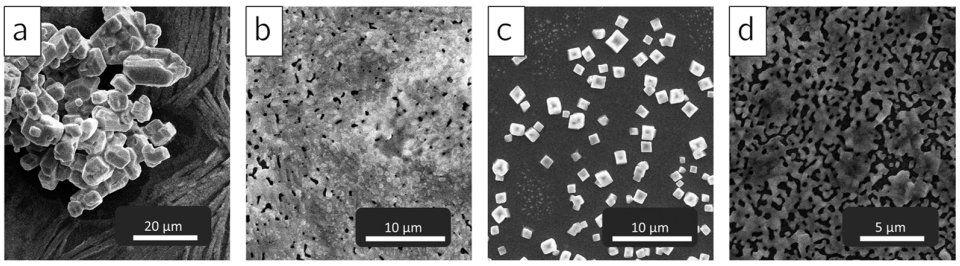

Figure 4.4: SEM top-view images of $CsPbBr_3$ thin films fabricated with a variety of state-of-the-art processing protocols. a) d) hot casting technique, requiring substrates at 300°C (adapted from [104]); b) one-step deposition, requiring a 0.3 M starting solution, with a DMF-based solvent annealing step during the thermal treatment (adapted from [105]); c) one-step deposition with low temperature annealing, resulting in a poor coverage of the substrate ([106]); d) one-step deposition, requiring a 0.15 M starting solution, with no solvent annealing (adapted from [105]). Scale bars are reported as reference.

a fully inorganic crystalline framework represents the most promising avenue for improving the thermal compositional stability [103], [105], which is important for real device operation. However, this specific material has been relatively unexplored up to now. This must be ascribed to the chemistry related to the Cesium precursor, CsBr. All the standard procedures for the crystallization of tri-dimensional bulk perovskites rely on the dissolution of the salt in DMF or DMSO, but CsBr exhibits a particularly low solubility even in these highly polar solvents. Since the thermodynamics of crystallization depends on the chemical formulation of the solution and its thermal treatment, the high level of control needed over the final thin film morphology and its opto-electronic properties, is extremely difficult to achieve. Conventional approaches can be employed, but compromises must be made. In Fig. 4.4 are reported top-view SEM images of thin films fabricated with a range of state-of-the-art processing protocols. To access these routes, it was necessary to significantly reduce the precursor concentration in order to dissolve the salt. Typically, precursor concentrations can vary between 1 to 1.6 M. In the case reported here, a concentration of 0.15 M was the highest achievable (Fig. 4.4, d). This produces thin films with very poor uniformity or extremely low optical density, completely unsuitable for device applications. Increasing the thickness or filling voids in the film using the same precursor solutions is currently not impossible with multiple cycles of depositions because they dissolve the layer formed in the previous step. Moreover, a thermal treatment over 250°C must be performed, otherwise either optically inactive phases or not-completely converted thin films are obtained. Thus, to date just few examples of $CsPbBr_3$-based devices have been reported. Conversely, as showed in Fig. 4.5, c, the NC ink approach offers the unique advantage of obtaining compact, continuous and uniform thin film of orthorhombic $CsPbBr_3$ perovskite without any additional ther-

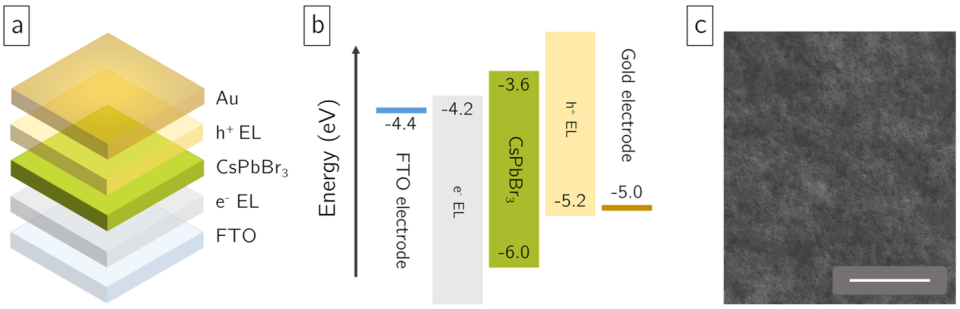

Figure 4.5: Scheme of the standard architecture of the solar cell, composed by a stacking of a transparent electrode (FTO), an electron extracting layer, the active material, a hole extracting layer and the evaporated metal electrode (Au). b) Energy-level diagram representing conduction band minimum and valence band maximum of the materials employed. The values are stated with respect to vacuum. c) Top-view SEM image of a single spin-coated layer of $CsPbBr_3$ NCs (scale bar 20 μm).

mal treatment.

To test the electronic performances of such inks, a state-of-the-art architecture have been chosen. Namely, a stack comprised of fluorine doped tin oxide (FTO) glass, a compact layer of titanium dioxide (c-TiO_2) as the electron-extracting layer, a layer of 2,20,7,70-tetrakis-(N,N-pdimethoxyphenylamino)-90- spirobifluorene (Spiro-MeOTAD) as the hole-transporting material and evaporated Au as the top contact. In Fig. 4.5, a and b, a sketch of the device stack is presented, as the energy levels of each layer selected, reporting literature values. To determine the NC thin films energy levels for the conduction and valence band, ultraviolet photo-electron spectroscopy (UPS) analysis is carried out (the measurement has been performed by Dr. Mirko Prato, IIT, Genova). The solar cell, in this case, exhibited a short-circuit current (J_{SC}) value of 1.26 mA/cm^2, an open-circuit voltage (V_{OC}) of 0.87 V, and a fill factor (FF) of 65%, for a power conversion efficiency (PCE) of 0.72%. The measured optical density for this film is limited to 0.3, as in Fig. 4.6, a. Nevertheless, both FF and V_{OC} values suggest a good electronic quality for such an extremely thin layer. The photo-current, however, is limited, accordingly to the reduced absorption. This can be increased preparing a thicker film, by performing sequential deposition cycles of the ink. This process, uniquely facilitated by the choice of a low boiling point solvent for the dispersion, enables a fast drying of the film after each deposition step, with no need to thermally treat the deposited material. Moreover, the organic molecule which acts as ligand for the particles, namely butylamine, can be easily removed by evaporation already at room temperature. By increasing the film thickness through sequential depositions, the optical density of the sample grows monotonically, while the NCs maintained their structural properties, as proved by comparing the XRD patterns of films obtained by spin-coating and by drop-casting. As reported in Fig. 4.6, b, increasing

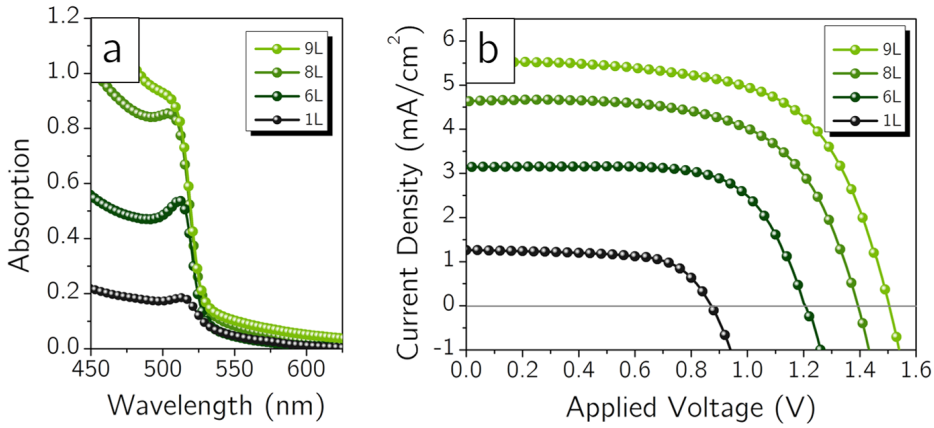

Figure 4.6: Multiple layer deposition effects. a) Optical absorption of increasingly thicker active layers, going from a single layer up to nine sequential deposition cycles (L). b) J-V characteristics of correspondent photovoltaic devices prepared by multiple deposition cycles.

the number of NC deposition cycles led to a direct increase of the optical thickness of the active layer, which is beneficial both for the J_{SC} and V_{OC} of the related devices. The FF remains almost constant, as reported in Table 4.1.The optimum has been achieved with an active layer of 550 ± 50 nm, prepared with nine multiple depositions. The solar cell present a J_{SC} and a V_{OC} values of 5.6 mA/cm^2 and 1.52 V, as well as a FF of 62%. The V_{OC} recorded is among the highest reported for all perovskite halides, underlining the high opto-electronic quality of the crystalline material synthetized. With this thickness, a PCE of 5.4% is measured, which is comparable to the best-performing and fully optimized wide-band-gap perovskite-based devices reported so far [107],[108]. As a reference, the ideal J-V characteristics of a solar cell based on an active layer with a band-gap identical to $CsPbBr_3$ (2.38 eV), reported a maximum V_{OC} and J_{SC} of 2.05 V and 7.78 mA/cm^2, respectively.

The measurements just mentioned have been performed employing an excitation with a simulated AM 1.5G spectrum (mismatch factor of 0.99) at 1 sun intensity. The voltage step and delay time are 10 mV and 10 ms, respectively, for a scan rate of 1 V/s. The voltage scan is imposed from 1.8 V to -0.2 V, with a pre-conditioning step consisting in 5 s light exposure at 1.8 V. Given these parameters, a dependence of the J-V characteristics on the polarization hystory of the devices is expected, if the direction of the scan rate is inverted (Fig. 4.7, a). As known, the use of TiO_2 as the electron-extracting layer in a flat-junction architecture generally presents the so-called electrical hysteresis. Usually, for $MAPbI_3$-based solar cells, under polarization, a reduction of the photo-current over time is observed [110]. Interestingly, in this case, decreasing the scan rate from 1 V/s to 0.1 V/s

Layers	J_{SC} (mA/cm^2)	V_{OC} (V)	FF (%)	PCE (%)
1	1.385	0.845	57.5	0.67
2	1.836	0.942	65.0	1.12
3	3.182	1.151	62.7	2.30
6	3.964	1.209	52.1	2.50
7	4.090	1.405	63.8	3.67
8	4.367	1.403	63.9	3.91
9	5.653	1.536	62.4	5.42
10	5.369	1.448	56.5	4.39
12	5.512	1.505	62.8	5.20
14	5.289	1.455	61.4	4.73

Table 4.1: Performances of the NCs-based perovskite solar cells, depending on the number of the deposited layers, measured at 1 sun intensity. The voltage step and delay time are 10 mV and 10 ms, respectively, for a scan rate of 1 V/s. The voltage scan is imposed from 1.8 V to -0.2 V. Pre-conditioning of the devices consists in 5 s of light exposure at 1.8 V.

induces an opposite behaviour than expected: an increase in the overall performances is registered, even though the device results more stressed under these conditions. Moreover, the devices show a rapid response of the photocurrent under polarization, resulting in electrically stable steady-state power output, as reported in Fig. 4.7, b and c.

Although the results achieved are impressive for such an easy process, allowing state-of-the-art PCEs and extremely high V_{OC}s, further optimization of the ink formulation can be done. Specifically, it is crucial to understand the role of many synthetic parameters in the crystallization process. Is it possible to control the perovskite domain size? Is this size influencing the J-V characteristics? Which parameters are directly linked to the aggregation level obtained for the crystals? To answer these questions, with the aim of increasing the power conversion efficiency of the final device, many aspects of the ink formulation can be investigated. Starting from the demonstration of the scalability of the volumes involved, the optimization will then probe the effect of the polarity of the nucleation environment and the role of the precursor concentration during the injection step. In addition, from the industrialization point-of-view, it is well known that the deposition method employed (i.e. spin-coating) is not optimal to obtain high uniformity over larger substrates. In fact, to achieve working devices with active areas of 1 cm^2, printing methods can offer many advantages. Nevertheless, the ink formulation employed in the just-reported case may not be suitable for such methodology, thus, a finer tuning of the ink's properties is required. The results of such investigation will be discussed in the next section. It is worth to noticed that the final goal is the realization of a hysteresis-free printed device, which will be presented in the final part of the following section.

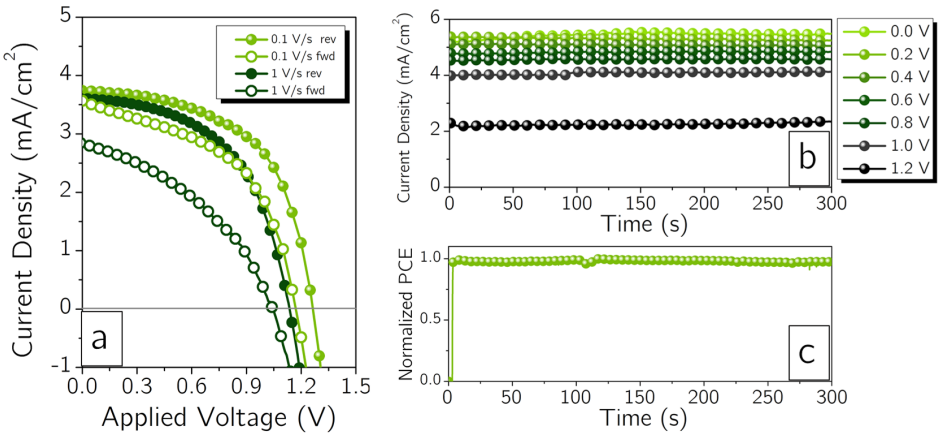

Figure 4.7: Performances of the NCs-based perovskite solar cells. a) Hysteresis of the devices depending on the scan rate of the applied voltage. At 0.1 V/s (light green) the electrical hysteresis is reduced, and the overall performances of the cells increase in respect to the behaviour measured for a scan rate of 1 V/s (dark green). The voltage applied from 1.8 V to -0.2 V is identified as 'reverse' (rev), while 'forward' (fwd) is the opposite direction. b) Transient photo-current density upon different polarizations, from 0 V to 1.2 V, for 300 s. c) Normalized PCE at maximum power point measured through MPP-tracking method.

4.4 Ink optimization for printed active layers

4.4.1 Ink's volume

Since the ultimate goal is the large-scale production compatibility, a first step is the demonstration of the reproducibility of the synthesis at the gram-scale. Thanks to the work of Q. A. Akkerman at IIT in Genova, this step has been achieved, as shown in Fig. 4.8. In fact, simple scaling of the quantities involved in the synthesis is sufficient to reproduce the high quality crystalline perovskite. To prove this, the absorption spectra, as well the XRD patterns of inks obtained at different volume scales have been investigated. They present the same features, confirming that this process is robust and reproducible in large quantities.

4.4.2 Ink's formulation

A second step in the optimization, is represented by a finer investigation of the role played by the details of the ink formulation. In fact, although this synthesis is straightforward, several parameters come into play. These are influencing both the crystallization dynamics and the stability of the colloidal suspension, as they act directly on the subsequent deposition conditions. Thus, it is important to remember that the recipe variations here reported have been tested with the final goal of increasing the overall power-conversion efficiency of the bar-coated devices, that will be presented in the next section.

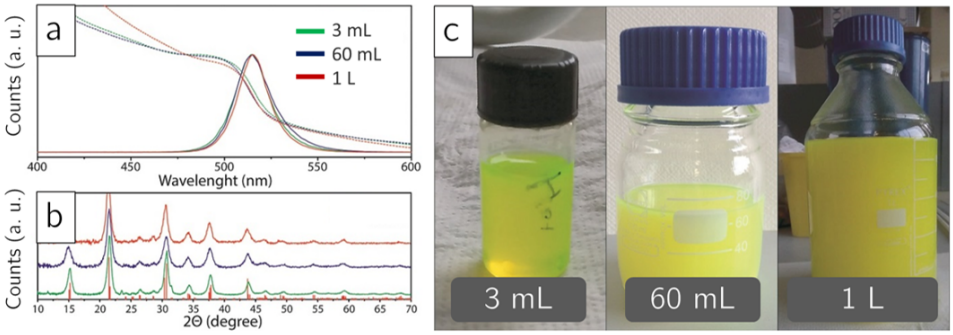

Figure 4.8: Characterization of NC inks during the scale-up process, for 3 ml solution (green), 60 ml (blue) and 1 L (red). a) Absorption spectra of the samples; b) XRD patterns; c) photos of the ink suspensions. The analysis has been performed by Q. A. Akkerman (IIT, Genova).

While, in the following, the active layer has been deposited by spin coating.

1. Polarity of the nucleation environment

The variation of the polarity of the nucleation environment, i.e. the volume ratio between IPA and HEX chosen, leads to a modification in the mean crystalline domain sizes of the particle obtained. The effect of this variation is reported in Fig. 4.9. As clearly shown in the first panel, in which TEM images of two different samples are reported, the average crystal domain size increases for more polar environments, going from an averaged value of less than 15 nm (HEX : IPA = 3 : 1) to more than 40 nm (HEX : IPA = 1 : 1). This averaged value is to be compared to the one reported in the previous section (Fig. 4.2), of 15 - 20 nm for the ratio HEX : IPA = 2 : 1. Accordingly to the increased average size, the absorption spectrum onset shift to longer wavelengths (Fig. 4.9, b) as the PL emission peak (Fig. 4.9, c).

2. Polarity of the re-dispersion solvent

The colloidal stability of the suspension can be affected varying the polarity of the solvent chosen to re-disperse the particles after the centrifugation step. Compared to IPA, less polar solvents, as Chlorobenzene (CB) and Toluene (TOL), favour the colloidal stability. As demonstrate previously, TOL represent the best choice for spin-coating deposition, even if CB creates colloidally more stable suspensions, maybe due to a better interaction with BuAm molecules. However, the PCE efficiencies of the CB-based devices are lower than the TOL-based ones. The difficulties encountered in the deposition of CB-based inks is due to the higher boiling point of the solvent itself, which hampers the fast drying of the thin film needed to control the final active layer thickness and its homogeneity. Thus, *per se*, a

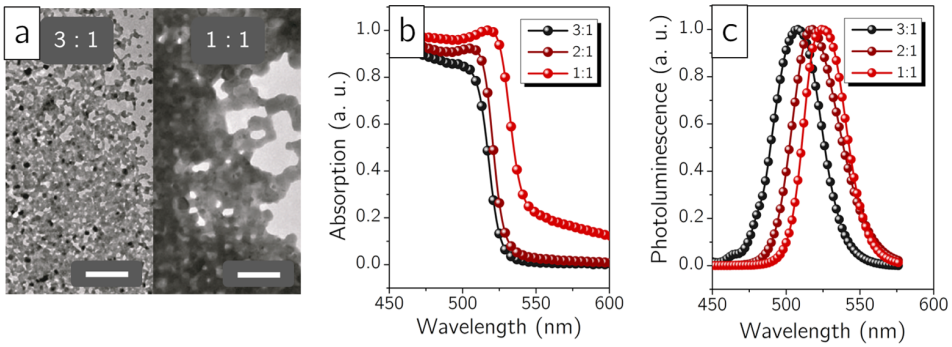

Figure 4.9: a) TEM images of two drop-casted samples obtained varying the ratio between HEX and IPA (scale bars 100 nm, measurement performed by Dr. G Bertoni). b) Normalized absorption spectra of the solutions. c) PL spectra of the same samples. A red-shift of the emission peak is recorded for larger particles, in accordance with the shift in the absorption edge, since the nucleation occurs in a more polar environment.

pre-aggregation of the suspended particles can represent an advantage during the deposition, allowing thicker and more homogeneous films. At the same time, if the polarity is increased further, as in the case of IPA-based inks, the suspension becomes excessively aggregated prior the deposition, and non-uniform coverage is obtained, affecting the overall performances of the photovoltaic devices. These effects can be observed in Fig. 4.10, in which normalized absorption spectra, XRD features and J-V characteristics of the so-obtained devices are reported. Thanks to the Scherrer equation [111], it is possible to calculate the average crystallite dimensions: for the TOL sample it results 18.30 ± 1.98 nm, for CB 19.33 ± 2.02 nm and for IPA the value increases to 33.22 ± 3.06 nm. The J-V curves are obtained with a scan rate of 1 V/s.

3. Concentration of precursors solutions

The relative concentration and volume of the two precursor solution injected can be tuned, leading to the crystallization of different particle sizes. As demonstrated in the previous Chapter for $MAPbI_3$, decreasing the molar concentration of the precursors in the crystallization environment translates into larger perovskite domains. To decrease the amount of lead reacting with the Cs-precursor without affecting other parameters, a series of different $PbBr_2$ solutions is prepared. The standard recipe requires $PbBr_2$ to be dissolved in a mixture of IPA, PrAc and BuAm, for a concentration of 0.5 M. The volume ratio for the solvents is fixed at IPA : PrAc : BuAm = 1 : 1 : 1. In this analysis, this ratio is kept constant, while progressively less powder is dissolved, starting from 18.35 mg/ml to 7.32 mg/ml, giving 5 different concentrations to be tested. The final effect is the synthesis of different inks with various mean crystallite sizes. The increase in the domain exten-

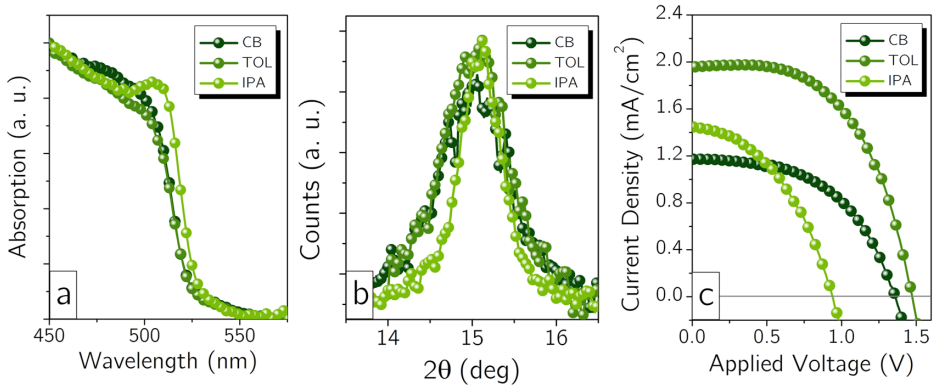

Figure 4.10: Dependence from the choice of the re-dispersion solvent for a) the absorption spectra, b) XRD main peaks, and c) J-V characteristics of related devices. Three solvents have been analyzed: Chlorobenzene (CB, dark green), Toluene (TOL, green) and Isopropanol (IPA, light green). The polarity of the solvents increases going from CB to IPA.

sion can be observed both in the absorption spectra and in the variation of the FWHM of the XRD peaks, which become smaller as the particles grow (Fig. 4.11, a and b). From the latter, it is possible to retrieve the average crystallite dimensions of the samples, which is reported in the Table 4.2. The characteristics of the photovoltaic devices show an interesting trend: as the particles grow, the measured J_{SC} constantly increases, and the increment seems to be limited only by the morphology of the deposited film. As showed in Fig. 4.12, in fact, the ink prepared with a diluted lead precursor solution (7.32 mg/ml) produces very inhomogeneous films, composed by larger crystallites. Thus, it is difficult to handle the material with a standard deposition technique, such as spin-coating. Rough surfaces and non-complete coverages are obtained. Thus, the depositions of the subsequent layers, i. e. the hole-transporting material and the evaporated electrode result highly discontinuous, hampering the correct charge-collection. Moreover, the V_{OC} increases up to the devices made with 13.21 mg/ml $PbBr_2$, which present the best J-V curve, while progressively decreases afterwards. The figures of merit of all the devices are reported in the Table 4.2. For these measurements, the voltage step and delay time are 10 mV and 10 ms, respectively. The voltage scan is imposed from 1.8 V to -0.2 V, with a pre-conditioning step consisting in 5s light exposure at 1.8 V. In conclusion, from the ink formulation point-of-view, the best results are obtained with the same nucleation environment conditions (polarity given by a HEX to IPA ratio of 2 to 1), the same re-dispersion solvent (TOL), and a decreased $PbBr_2$ precursor concentration (13.21 mg/ml, to obtain the most advantageous trade-off between an increased J_{SC} and the surface roughness of the perovskite layer).

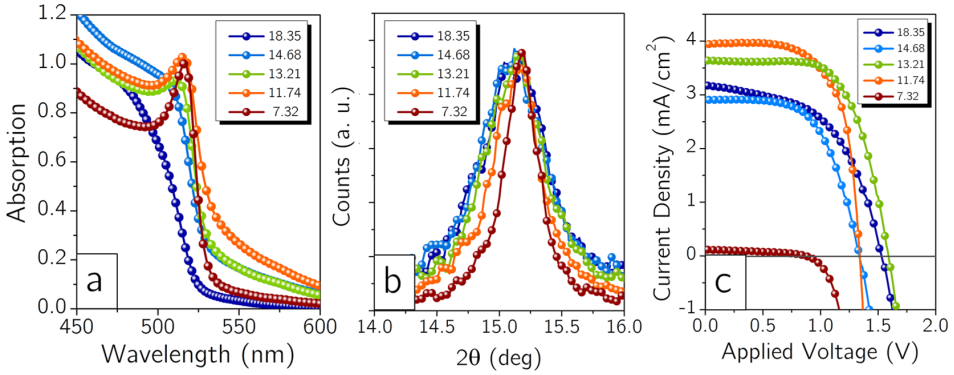

Figure 4.11: $PbBr_2$ concentration dependence analysis (values expressed in mg/ml), reported in a) the absorption spectra and in b) XRD patterns and c) J-V characteristics of solar cells of NCs made starting from different concentration of the lead precursor solution (from 18.35 mg/ml to 7.32 mg/ml). Decreasing the concentration, the performances increase, with the best cells given by a starting solution of 13.21 mg/ml of $PbBr_2$.

$PbBr_2$ conc. (mg/ml)	Mean domain size (nm)	J_{SC} (mA/cm^2)	V_{OC} (V)	FF (%)	PCE (%)
18.35	18.32	3.17	1.53	53.2	2.59
14.68	23.66	2.90	1.34	60.1	2.37
13.21	28.26	3.63	1.60	64.3	3.73
11.74	38.55	3.94	1.34	66.2	3.56
7.32	60.40	0.13	0.88	39.6	0.04

Table 4.2: Figures of merit of the solar cells presented in Fig.4.11. For each lead precursor starting concentration, the average crystallite dimension is reported. For the J-V curves, the voltage is applied from 1.8 V to -0.2 V, with a scan rate of 1 V/s.

4.4.3 Ink's deposition

Finally, the ink employment opens new strategies for the deposition method. In this case, a technique compatible with large-area substrates and high-throughput is desirable. As a matter of fact, spin-coating method is extremely useful for small active area and lab-scale production. Thus, an investigation over bar-coated perovskite thin film is performed. Bar-coating is a simple and scalable printing technique, often used in polymer-based technology: it consists in a grooved metal bar placed in contact with the substrate, which is covered by the ink. Once the movement of the bar is triggered, the ink is spread on the substrate. The final layer thickness can be controlled through a combination of factors, such as the viscosity of the ink, its concentration, the speed of the bar and the pitch of the grooves selected [112], [113].

To be consistent, as mentioned previously, the device stack is kept the

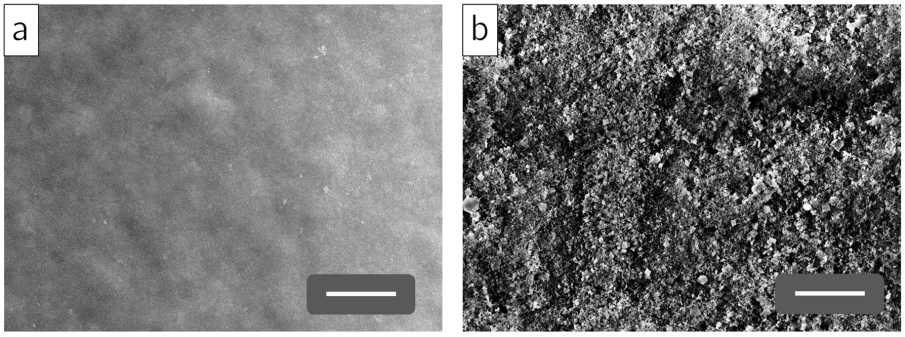

Figure 4.12: Top-view SEM images of two representative samples for the lead-concentration dependence analysis. a) Thin film obtained from the deposition of the ink prepared with 18.32 mg/ml $PbBr_2$ precursor solution, and b) the one from the 7.32 mg/ml precursor solution. Scale bars of 5 μm. Higher roughness hamper the uniformity of the layers deposited on top, reducing the overall efficiency of the solar cells.

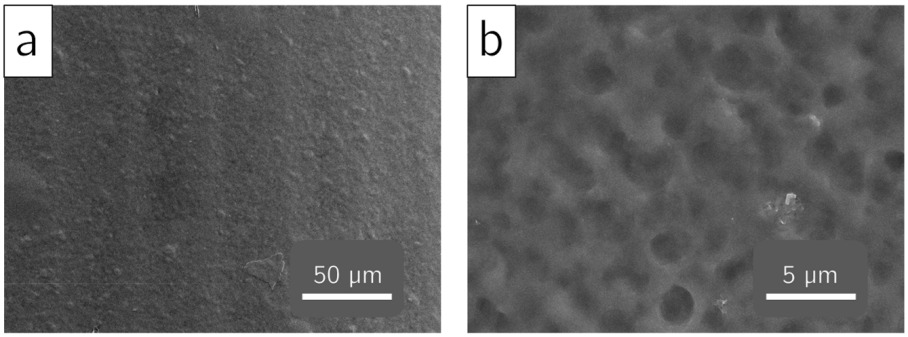

Figure 4.13: Top-view SEM images of bar-coated thin films, with different scale bars. The coverage of the substrate is sufficiently homogeneous to obtain working devices, but the roughness of the surface is higher than the one obtained by spin-coating.

same, while the different ink formulations are studied. Here will be reported the best results obtained, for the 13.21 mg/ml $PbBr_2$ precursor dispersed in TOL. Full coverage and the correct optical thickness are guaranteed by 3 subsequent bar-assisted depositions. In this case, 100 μl of perovskite nanocrystals is spread at one border of the substrate, close to the metal bar. The bar speed which gives the best result, in terms of homogeneity of the final film, is set to 30 μm/s. In Fig. 4.13, two top-view SEM images are reported, showing the morphology of the so-obtained thin film. In Fig. 4.14, the characterization, comparing the two deposition methods, is presented: starting from the absorption spectra, to the XRD features and the J-V curves, the same TOL-based ink is performing differently. In particular, even if the optical thickness is comparable (Fig. 4.14, a), the spin-coated films perform better. Up to the time this thesis have been completed, no unambiguous and coherent explanation for this phenomenon is available.

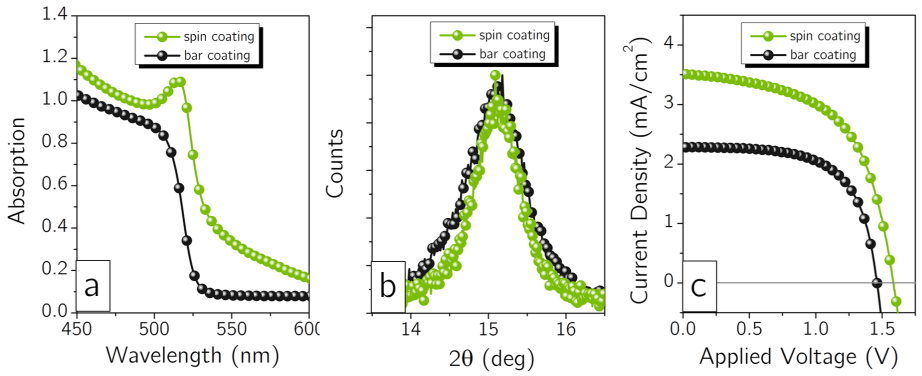

Figure 4.14: Bar- vs. spin-coating deposition techniques. a) Absorption spectra, b) XRD measurements and c) J-V characteristics of solar cells obtained with the same $CsPbBr_3$ ink formulation.

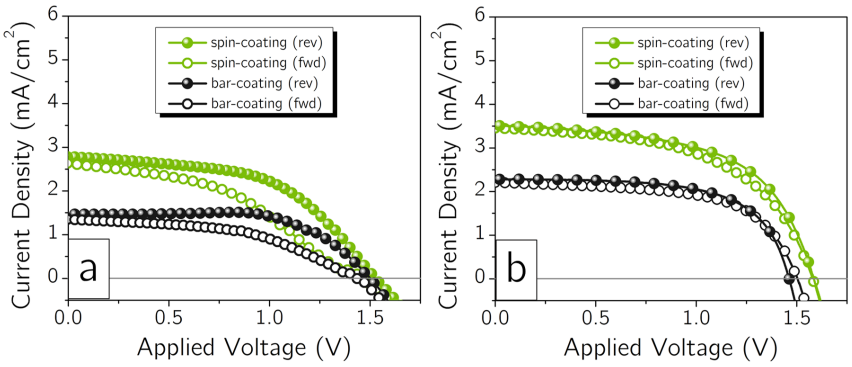

Figure 4.15: Bar- vs. spin-coating deposition techniques. a) J-V curves of $CsPbBr_3$ solar cells measured with fast scan rates (1 V/s) and a pre-conditioning step of 10 s light exposure at 1.8 V. b) J-V curves for devices measured at a slower scan rate (0.1 V/s) with a pre-conditioning step of 10 s in light (no bias).

Further investigations would be needed: for example, a HR-SEM analysis of the layer-by-layer deposited perovskite could show if any modification over the aggregation of the particles on the substrate is occurring; or a more detailed XRD studies could perhaps indicate if an alteration in the symmetry of the lattice is present, maybe provoked by the mechanical stress induced by the metal bar action. Undoubtedly, the most interesting data comes from the analysis over the polarization-induced electrical instability. The optimized ink formulation shows less hysteresis compared to the previous case (Fig. 4.7). Best results are observed when the devices are measured with a scan rate of 0.1 V/s, with a pre-conditioning step of 10 s in light, without any bias applied. A detailed comparison of the figures of merit of these devices is reported in Table 4.3.

Deposition method	Scan direction	Scan rate (V/s)	Pre-bias (V)	J_{SC} (mA/cm^2)	V_{OC} (V)	FF (%)	PCE (%)
spin-coating	rev	1	1.8	2.79	1.53	52.2	2.29
spin-coating	fwd	1	1.8	2.63	1.46	0.41	1.73
spin-coating	rev	0.1	n. a.	3.52	1.58	57.2	3.29
spin-coating	fwd	0.1	n. a.	3.46	1.58	54.0	3.04
bar-coating	rev	1	1.8	1.47	1.50	64.9	1.47
bar-coating	fwd	1	1.8	1.36	1.43	47.7	0.96
bar-coating	rev	0.1	n. a.	2.28	1.46	64.2	2.20
bar-coating	fwd	0.1	n. a.	2.21	1.50	60.9	2.08

Table 4.3: Figures of merit of the solar cells presented in Fig.4.15. A comparison between different deposition methods and different measurement settings is presented: reverse- ('rev', voltage applied from 1.8 V to -0.2 V) versus forward-scan ('fwd', from -0.2 V to 1.8 V); scan rates of 1 or 0.1 V/s; pre-conditioning step of 10 s light exposure with versus without bias. In the case of no-bias and slower scan rate, the electrical hysteresis is highly reduced in both spin- and bar-coated perovskite thin films.

Chapter 5

Conclusion and perspectives

Since their introduction as photo-active materials in solar cells, tri-dimensional lead halide perovskite semiconductors led to great advances in the performances of this technology. This class of materials are an emerging solution-processed that has demonstrated good potential even when embodied in light emitting devices and photodetectors, thanks to the exceptional opto-electronic properties. At the same time, many of the finer details of the device physics remain under debate, in particular, the role of structural and chemical defects, and their effects on the properties of devices.

Overall, the three-year work highlights the primary properties of the same class of material obtained by various synthetic routes, combining structural and morphological characterizations to the photo-physical ones. The results reported shows a direct comparison between two different approaches to the realization of a perovskite-based thin film. The first one consists in the direct crystallization of the semiconductive material onto a substrate, starting from precursors solutions, while the second one relies on the deposition of pre-formed high-quality colloidal perovskite-based nanocrystals. The first approach is the most widely used in literature, however, chemical purity of the precursors, presence of additives, relative humidity, temperature and surface properties of the substrates employed can deeply affect the organization of the perovskite crystalline lattice. In this case, a non-negligible level of unintentional structural and chemical defects is created, both within the bulk and at the interfaces of the crystals. Such defects can introduce localized energy levels that are confined in the band-gap of the semiconductor, creating non-radiative recombination pathways for the photo-generated charge carriers. A reproducible and reliable protocol to fabricate polycrystalline thin film, with different average-crystallite dimensions, is reported. Varying the crystallites mean size, from tens of nanometers to a few micrometers, it is possible to tune the opto-electronic behaviour of the material, directly influencing the number and the type of electrically-active defect sites. From these results, the existence of a tight tolerance window for the optimal processing

parameters of these self-assembled materials clearly emerges.

A novel approach is then proposed, consisting in the realization of the solar cell active layer by the deposition of an ink composed by suspended nanoparticles. The ink formulation can be tailored prior to the film formation, meaning that the co-optimization of large-area uniform coverage with a high-quality crystal growth is no longer needed. The results obtained by following this approach are presented in the second part of the thesis. A fully inorganic cesium lead bromide perovskite has been employed in the study, thanks to a new, fast and one-step-injection synthesis. The use of ligands, composed by short alkyl chains, circumvents post-synthesis treatments typical of the longer and bulkier chains usually employed in this field. The passivating nature of the ligands gives rise to extremely good photo-luminescence properties, a good fingerprint of the optical and structural quality of the perovskite lattice obtained. The inks are then used to fabricate a halide perovskite nanocrystalline-based photovoltaic prototype device, achieving power-conversion efficiencies comparable to the best-performing and fully optimized devices reported so far. Finally, a finer analysis over the role of the synthetic parameters in the device performances has been proposed, with the aim of demonstrating the validity of this approach by successfully applied it to large-area deposition techniques, to fabricate hysteresis-free solar cells. However, the performances of such printed devices is limited by the current extracted, while the V_{OC}s are among the highest ever reported to date. It is worth mentioning that, although there are several factors that determine the V_{OC} and their contribution is still an open issue in the field, literature reports seem to suggest that further improvements will be possible by carefully designing the charge-extracting layers, highlighting the potential of our approach.

To conclude, the understanding of the limiting material properties is constantly growing. For future efforts, an important area of focus is the control of defects, which have an impact on several aspects of the semiconductor itself, and of course, on the related device functionality. The ability to grow high electronic quality crystals and thin films will be the basis to achieve further improvements in the efficiency of perovskite-based opto-electronic devices. Therefore, with greater control over the engineering of the thin films, solar cell power conversion efficiencies can be expected to continue to approach their thermodynamic limit.

Bibliography

[1] A. Luque, S. Hegedus, *Handbook of Photovoltaic Science and Engineering*, Wiley-VCH, 2013.

[2] P. Würfel, *The Chemical Potential of Radiation*, J. Phys. C - Solid State Physics, 15, 3967, 1982.

[3] P. Stallinga, *Electrical Characterization of Organic Electronic Material and Devices*, Wiley-VCH, 2009.

[4] M.A. Pena, J.L.G. Fierro, *Chemical Structures and Performance of Perovskite Oxides*, Chem. Rev. 101, 1981—2017, 2001.

[5] C.K. Moller, *Crystal Structure and Photoconductivity of Cesium Plumbohalides*, Nature 182, 1436, 1958.

[6] D. Weber, *$CH_3NH_3PbX_3$, ein Pb(II)-System mit kubischer Perowskitstruktur*, Inst. Anorg. Chem. Univ. Stutt. 33b, 1443—1445, 1978.

[7] D.B. Mitzi, *Synthesis, structure, and properties of organic-inorganic perovskites and related materials*, Prog. Inorg. Chem. 48, 1-121, 2007.

[8] A. Kojima, K. Teshima, T. Miyasaka, Y. Shirai, *Organo lead halide perovskite for high efficiency printable solar cells and optoelectronic devices*, Proc. 210^{th} ECS Meeting, ECS, 2006.

[9] A. Kojima, K. Teshima, Y. Shirai, T. Miyasaka, *Organometal Halide Perovskites as Visible-Light Sensitizers for Photovoltaic Cells*, J. Am. Chem. Soc., 131, 6050, 2009.

[10] National Renewable Energy Laboratory, *Best Research-Cell Efficiencies chart*, `https://www.nrel.gov/pv/assets/ images/efficiency-chart.png`.

[11] Nakita K. Noel, S. D. Stranks, A. Abate, C. Wehrenfennig, S. Guarnera, A. Haghighirad, A. Sadhanala, G. E. Eperon, S. K. Pathak, M. B. Johnston, A. Petrozza, L. Herz, and H. J. Snaith. *Lead-Free Organic-Inorganic Tin Halide Perovskites for Photovoltaic Applications.* Energy & Environmental Science, 7:3061-3068, 2014.

[12] F. Hao, C. C. Stoumpos, D. H. Cao, R. P. H. Chang, and M. G. Kanatzidis. *Lead-free solid-state organic-inorganic halide perovskite solar cells*, Nature Photonics, 8(6):489-494, 2014.

[13] V. M. Goldschmidt, *Die Gesetze der Krystallochemie*, Naturwissenschaften, 14, 477, 1926.

[14] G. Kieslich, S. Sun, A. K. Cheetham, *Solid-state principles applied to organic-inorganic perovskites: new tricks for an old dog*, Chem. Sci., 5, 4712, 2014.

[15] G. Kieslich, S. Sun, A. K. Cheetham, *Role of entropic effects in controlling the polymorphism in formate ABX_3 metal–organic frameworks*, Chem. Sci. 6, 3430, 2015.

[16] S. A. Veldhuis, P. P. Boix, N. Yantara, M. Li, T. C. Sum, N. Mathews, S. G. Mhaisalkar, *Perovskite Materials for Light-Emitting Diodes and Lasers*, Adv. Mater. 28, 6804, 2016.

[17] T. Baikie, Y. Fang, J. M. Kadro, M. Schreyer, F. Wei, S. G. Mhaisalkar, M. Graetzel, and T. J. White. *Synthesis and crystal chemistry of the hybrid perovskite $(CH_3NH_3)PbI_3$ for solid-state sensitised solar cell applications*, Journal of Materials Chemistry A, 1(18):5628, 2013.

[18] M. R. Filip, G. E. Eperon, H. J. Snaith, F. Giustino, *Steric engineering of metal-halide perovskites with tunable optical band gaps*, Nature communications, 5:5757, 2014.

[19] H. Tsai, W. Nie, J.-C. Blancon, C. C. Stoumpos, R. Asadpour, B. Harutyunyan, A. J. Neukirch, R. Verduzco, J. J. Crochet, S. Tretiak, L. Pedesseau, J. Even, M. A. Alam, G. Gupta, J. Lou, P. M. Ajayan, M. J. Bedzyk, M. G. Kanatzidis and A. D. Mohite, *High-efficiency two-dimensional Ruddlesden-Popper perovskite solar cells*, Nature 536, 2016.

[20] C. C. Stoumpos, D. H. Cao, D. J. Clark, J. Young, J. M. Rondinelli, J. I. Jang, J. T. Hupp, M. G. Kanatzidis, *Ruddlesden–Popper Hybrid Lead Iodide Perovskite 2D Homologous Semiconductors*, Chem. Mater., 28, 2852, 2016.

[21] L. N. Quan, M. Yuan, R. Comin, O. Voznyy, E. M. Beauregard, S. Hoogland, A. Buin, A. R. Kirmani, K. Zhao, A. Amassian, *Ligand-Stabilized Reduced-Dimensionality Perovskites*, J. Am. Chem. Soc., 138, 2649, 2016.

[22] Q. Chen, N. De Marco, Y. M. Yang, T. B. Song, C. C. Chen, H. Zhao, Z. Hong, H. Zhou, Y. Yang, *Under the spotlight: The organic–inorganic hybrid halide perovskite for optoelectronic applications*, Nano Today, 10(3):355–396, 2015.

[23] T. Leijtens, G. E. Eperon, N. K. Noel, S. N. Habisreutinger, A. Petrozza, H. J. Snaith, *Stability of metal halide perovskite solar cells*, Adv. Energy Mater., 5, 1500963, 2015.

[24] T. M. Koh, K. Thirumal, H. S. Soo, N. Mathews, *Multidimensional Perovskites: A Mixed Cation Approach Towards Ambient Stable and Tunable Perovskite Photovoltaics*, ChemSusChem, 9, 2541, 2016.

[25] G. Niu, X. Guo, L. Wang, *Review of recent progress in chemical stability of perovskite solar cells*, J. Mater. Chem. A, 3, 8970, 2015.

[26] B. Conings, J. Drijkoningen, N. Gauquelin, A. Babayigit, J. D'Haen, L. D'Olieslaeger, A. Ethirajan, J. Verbeeck, J. Manca, E. Mosconi, F. D. Angelis, H.-G. Boyen, *Intrinsic Thermal Instability of Methylammonium Lead Trihalide Perovskite*, Adv. Energy Mater., 5, 1500477, 2015.

[27] W. Shockley, H. J. Queisser, J. Appl. Phys., *Detailed Balance Limit of Efficiency of p-n Junction Solar Cells* 32, 510, 1961.

[28] A. Amat, E. Mosconi, E. Ronca, C. Quarti, P. Umari, M. K. Nazeeruddin, M. Grätzel, F. De Angelis, *Cation-Induced Band-Gap Tuning in Organohalide Perovskites: Interplay of Spin-Orbit Coupling and Octahedra Tilting* Nano Lett., 14, 3608, 2014.

[29] J. W. Lee, D. J. Seol, A. N. Cho, N. G. Park, *High-efficiency perovskite solar cells based on the black polymorph of $HC(NH_2)_2PbI_3$*, Adv. Mater., 26, 4991, 2014.

[30] C. C. Stoumpos, C. D. Malliakas, M. G. Kanatzidis, *Semiconducting tin and lead iodide perovskites with organic cations: phase transitions, high mobilities, and near-infrared photoluminescent properties*, Inorg. Chem., 52, 9019, 2013.

[31] M. Kulbak, D. Cahen, G. Hodes, *How Important Is the Organic Part of Lead Halide Perovskite Photovoltaic Cells? Efficient $CsPbBr_3$ Cells*, J. Phys. Chem. Lett., 6, 2452, 2015.

[32] M. Yang, T. Zhang, P. Schulz, Z. Li, G. Li, D. H. Kim, N. Guo, J. J. Berry, K. Zhu, Y. Zhao, *Facile fabrication of large-grain $CH_3NH_3PbI_{3-x}Br_x$ films for high-efficiency solar cells via CH_3NH_3Br-selective Ostwald ripening* Nature Communications, 7, 12305, 2016.

[33] A. Poglitsch, D. Weber, *Dynamic disorder in methylammoniumtrihalogenoplumbates (II) observed by millimeter-wave spectroscopy* J. Chem. Phys., 87, 6373, 1987.

[34] J. H. Noh, S. H. Im, J. H. Heo, T. N. Mandal, S. I. Seok, *Chemical management for colorful, efficient, and stable inorganic-organic hybrid nanostructured solar cells* Nano Lett., 13, 1764, 2013.

[35] E. T. Hoke, D. J. Slotcavage, E. R. Dohner, A. R. Bowring, H. I. Karunadasa, M. D. McGehee, *Reversible photo-induced trap formation in mixed-halide hybrid perovskites for photovoltaics*, Chem. Sci., 6, 613, 2015.

[36] D. J. Slotcavage, H. I. Karunadasa, M. D. McGehee, *Light-Induced Phase Segregation in Halide-Perovskite Absorbers*, ACS Energy Lett., 1, 1199, 2016.

[37] D. Bi, W. Tress, M. I. Dar, P. Gao, J. Luo, C. Renevier, K. Schenk, A. Abate, F. Giordano, J.-P. C. Baena,*Efficient luminescent solar cells based on tailored mixed-cation perovskites*, Sci. Adv., 2, e1501170, 2016.

[38] M. Saliba, T. Matsui, J. Seo, K. Domanski, J. Correa-Baena, M. K. Nazeeruddin, S. M. Zakeeruddin, W. Tress, A. Abate, A. Hagfeldt, M. Gratzel, *Cesium-containing triple cation perovskite solar cells: improved stability, reproducibility and high efficiency*, Energy & Environmental Science 9 (6), 1989-1997, 2016.

[39] M. Saliba, T. Matsui, K. Domanski, J.-Y. Seo, A. Ummadisingu, S. M. Zakeeruddin, J.-P. Correa-Baena, W. R. Tress, A. Abate, A. Hagfeldt, *Cesium-containing triple cation perovskite solar cells: improved stability, reproducibility and high efficiency*, Science, 354, 206, 2016.

[40] G. E. Eperon, T. Leijtens, K. A. Bush, R. Prasanna, T. Green, J. Tse-Wei Wang, D. P. McMeekin, G. Volonakis, R. L. Milot, R. May, A. Palmstrom, D. J. Slotcavage, R. A. Belisle, J. B. Patel, E. S. Parrott, R. J. Sutton, W. Ma, F. Moghadam, B. Conings, A. Babayigit, H.-G. Boyen, S. Bent, F. Giustino, L. M. Herz, M. B. Johnston, M. D. McGehee, H. J. Snaith, *Perovskite-perovskite tandem photovoltaics with optimized band gaps*, Science, 354, 6314, 2016.

[41] N. Pellet, P. Gao, G. Gregori, T. Y. Yang, M. K. Nazeeruddin, J. Maier, M. Gratzel, *Mixed-organic-cation perovskite photovoltaics for enhanced solar-light harvesting*, Angew. Chem. Int. Ed., 53, 3151, 2014.

[42] J. Liu, Y. Shirai, X. D. Yang, Y. F. Yue, W. Chen, Y. Z. Wu, A. Islam, L. Y. Han, *High-Quality Mixed-Organic-Cation Perovskites from a Phase-Pure Non-stoichiometric Intermediate $(FAI)_{1-x}PbI_2$ for Solar Cells*, Adv. Mater., 27, 4918, 2015.

[43] G. E. Eperon, C. E. Beck, H. J. Snaith, *Cation exchange for thin film lead iodide perovskite interconversion*, Mater. Horiz., 3, 63, 2016.

[44] Z. Li, M. J. Yang, J. S. Park, S. H. Wei, J. J. Berry, K. Zhu, *Stabilizing Perovskite Structures by Tuning Tolerance Factor: Formation of Formamidinium and Cesium Lead Iodide Solid-State Alloys*, Chem. Mater., 28, 284, 2016.

[45] J. W. Lee, D. H. Kim, H. S. Kim, S. W. Seo, S. M. Cho, N. G. Park, *Formamidinium and Cesium Hybridization for Photo- and Moisture-Stable Perovskite Solar Cell*, Adv. Energy Mater., 5, 1501310, 2015.

[46] I. Chung, B. Lee, J. He, R. P. Chang, M. G. Kanatzidis, *All-solid-state dye-sensitized solar cells with high efficiency*, Nature, 485, 486, 2012.

[47] N. K. Noel, S. D. Stranks, A. Abate, C. Wehrenfennig, S. Guarnera, A.-A. Haghighirad, A. Sadhanala, G. E. Eperon, S. K. Pathak, M. B. Johnston, *Lead-free organic-inorganic tin halide perovskites for photovoltaic applications*, Energy Environ. Sci., 7, 3061, 2014.

[48] F. Hao, C. C. Stoumpos, D. H. Cao, R. P. Chang, M. G. Kanatzidis, *Lead-free solid-state organic-inorganic halide perovskite solar cells* Nat. Photonics, 8, 489, 2014.

[49] I. Chung, J. H. Song, J. Im, J. Androulakis, C. D. Malliakas, H. Li, A. J. Freeman, J. T. Kenney, M. G. Kanatzidis, *CsSnI3: Semiconductor or metal? High electrical conductivity and strong near-infrared photoluminescence from a single material. High hole mobility and phase-transitions* J. Am. Chem. Soc., 134, 8579, 2012.

[50] F. Brivio, A. B. Walker, A. Walsh, *Structural and electronic properties of hybrid perovskites for high-efficiency thin-film photovoltaics from first-principles*, APL Mater., 1, 042111, 2013.

[51] A. Walsh, *Principles of Chemical Bonding and Band Gap Engineering in Hybrid Organic-Inorganic Halide Perovskites*, J. Phys. Chem. C, 119, 5755, 2015.

[52] M. M. Lee, J. Teuscher, T. Miyasaka, T. N. Murakami, and H. J. Snaith, *Efficient hybrid solar cells based on mesosuperstructured organometal halide perovskites*, Science, 338(6107)643-7, 2012.

[53] P. Docampo, F. C. Hanusch, S. D. Stranks, M. Döblinger, J. M. Feckl, M. Ehrensperger, N. K. Minar, M. B. Johnston, H. J. Snaith, T. Bein, *Solution Deposition-Conversion for Planar Heterojunction Mixed Halide Perovskite Solar Cells*, Adv. Energy Mater., 4, 1400355, 2014.

[54] Y. Zhao, K. Zhu, *CH_3NH_3Cl-Assisted One-Step Solution Growth of $CH_3NH_3PbI_3$: Structure, Charge-Carrier Dynamics, and Photovoltaic Properties of Perovskite Solar Cells* J. Phys. Chem. C, 118, 9412, 2014.

[55] E. Edri, S. Kirmayer, A. Henning, S. Mukhopadhyay, K. Gartsman, Y. Rosenwaks, G. Hodes, D. Cahen, *Why Lead Methylammonium Tri-Iodide Perovskite-Based Solar Cells Require a Mesoporous Electron Transporting Scaffold (but Not Necessarily a Hole Conductor)* Nano Lett., 14, 1000, 2014.

[56] H. Yu, F. Wang, F. Xie, W. Li, J. Chen, N. Zhao, *The Role of Chlorine in the Formation Process of "$CH_3NH_3PbI_{3-x}Cl_x$" Perovskite*, Adv. Funct. Mater., 24, 7102, 2014.

[57] Z. Xiao, C. Bi, Y. Shao, Q. Dong, Q. Wang, Y. Yuan, C. Wang, Y. Gao, J. Huang, *Efficient, high yield perovskite photovoltaic devices grown by interdiffusion of solution-processed precursor stacking layers*, Energy Environ. Sci., 7, 2619, 2014.

[58] C. Eames, J. M. Frost, P. R. Barnes, B. C. O'regan, A. Walsh, M. S. Islam, *Ionic transport in hybrid lead iodide perovskite solar cells*, Nat. Commun. 6, 7497, 2015.

[59] J. S. Yun, J. Seidel, J. Kim, A. M. Soufiani, S. Huang, J. Lau, N. J. Jeon, S. I. Seok, M. A. Green, A. Ho-Baillie, *Critical Role of Grain Boundaries for Ion Migration in Formamidinium and Methylammonium Lead Halide Perovskite Solar Cells*, Adv. Energy Mater., 6, 1600330, 2016.

[60] A. J. Barker, A. Sadhanala, F. Deschler, M. Gandini, S. P. Senanayak, P. M. Pearce, E. Mosconi, A. J. Pearson, Y. Wu, A. R. S. Kandada, T. Leijtens, F. De Angelis, S. E. Dutton, A. Petrozza, R. H. Friend, *Defect-Assisted Photoinduced Halide Segregation in Mixed-Halide Perovskite Thin Films*, ACS Energy Lett., 2 (6), 1416–1424, 2017.

[61] W. Y. Liang, Phys. Educ., *Excitons*, 5, 226, 1970.

[62] J. Singh, *Excitation Energy Transfer Processes in Condensed Matter: Theory and Applications*, Springer US, Boston, 1, 1994.

[63] B. A. Gregg, M. C. Hanna, *Comparing organic to inorganic photovoltaic cells: Theory, experiment, and simulation*, J. Appl. Phys., 93, 3605, 2003.

[64] V. D'Innocenzo, G. Grancini, M. J. P. Alcocer, A. R. S. Kandada, S. D. Stranks, M. M. Lee, G. Lanzani, H. J. Snaith, A. Petrozza, *Excitons versus free charges in organo-lead tri-halide perovskites*, Nature Communications, 5, 2014.

[65] Q. Lin, A. Armin, R. C. R. Nagiri, P. L. Burn, P. Meredith, *Electro-optics of perovskite solar cells*, Nat. Photonics, 9, 106, 2015.

[66] M. De Bastiani, V. D'Innocenzo, S. D. Stranks, H. J. Snaith, A. Petrozza, *Role of the crystallization substrate on the photoluminescence properties of organo-lead mixed halides perovskites*, Apl Materials, 2 (8), 081509, 2014.

[67] J. H. Heo, S. H. Im, J. H. Noh, T. N. Mandal, C. S. Lim, J. A. Chang, Y. H. Lee, H. J. Kim, A. Sarkar, M. K. Nazeeruddin, M. Gratzel, S. I. Seok,

Efficient inorganic-organic hybrid heterojunction solar cells containing perovskite compound and polymeric hole conductors, Nat. Photonics, 7, 487, 2013.

[68] M. Xiao, F. Huang, W. Huang, Y. Dkhissi, Y. Zhu, J. Etheridge, A. Gray-Weale, U. Bach, Y. B. Cheng, L. Spiccia, *A fast deposition-crystallization procedure for highly efficient lead iodide perovskite thin-film solar cells*, Angew. Chem. Int. Ed., 53, 9898, 2014.

[69] M. Liu, M. B. Johnston, H. J. Snaith, *Efficient planar heterojunction perovskite solar cells by vapour deposition*, Nature, 501, 395, 2013.

[70] N. J. Jeon, J. H. Noh, Y. C. Kim, W. S. Yang, S. Ryu, S. I. Seok, *Solvent engineering for high-performance inorganic-organic hybrid perovskite solar cells*, Nat. Materials, 13, 897, 2014.

[71] Q. Chen, H. Zhou, Z. Hong, S. Luo, H.-S. Duan, H.-H. Wang, Y. Liu, G. Li and Y. Yang, *Planar heterojunction perovskite solar cells via vapor-assisted solution process* J. Am. Chem. Soc., 136, 622– 625, 2013.

[72] H. Cho, S.-H. Jeong, M.-H. Park, Y.-H. Kim, C. Wolf, C.-L. Lee, J. H. Heo, A. Sadhanala, N. Myoung, S. Yoo, S. H. Im, R. H. Friend, T.-W. Lee, *Overcoming the electroluminescence efficiency limitations of perovskite light-emitting diodes*, Science, 350, 1222, 2015.

[73] N. Ahn, D.-Y. Son, I.-H. Jang, S. M. Kang, M. Choi, N.-G. Park, *Highly Reproducible Perovskite Solar Cells with Average Efficiency of 18.3% and Best Efficiency of 19.7% Fabricated via Lewis Base Adduct of Lead(II) Iodide* J. Am. Chem. Soc., 137, 8696, 2015.

[74] J. Burschka, N. Pellet, S.-J. Moon, R. Humphry-Baker, P. Gao, M. K. Nazeeruddin, M. Gratzel, *Sequential deposition as a route to high-performance perovskite-sensitized solar cells*, Nature, 499, 316, 2013.

[75] K. Hwang, Y.-S. Jung, Y.-J. Heo, F. H. Scholes, S. E. Watkins, J. Subbiah, D. J. Jones, D.-Y. Kim, D. Vak, *Toward Large Scale Roll-to-Roll Production of Fully Printed Perovskite Solar Cells*, Adv. Mater., 27, 1241, 2015.

[76] A. T. Barrows, A. J. Pearson, C. K. Kwak, A. D. F. Dunbar, A. R. Buckley, D. G. Lidzey, *Efficient planar heterojunction mixed-halide perovskite solar cells deposited via spray-deposition*, Energy Environ. Sci., 7, 2944, 2014.

[77] S. Das, B. Yang, G. Gu, P. C. Joshi, I. N. Ivanov, C. M. Rouleau, T. Aytug, D. B. Geohegan, K. Xiao, *High-Performance Flexible Perovskite Solar Cells by Using a Combination of Ultrasonic Spray-Coating and Low Thermal Budget Photonic Curing*, ACS Photonics, 2, 680, 2015.

[78] Y. Deng, E. Peng, Y. Shao, Z. Xiao, Q. Dong, J. Huang, *Scalable fabrication of efficient organolead trihalide perovskite solar cells with doctor-bladed active layers*, Energy Environ. Sci., 8, 1544, 2015.

[79] X. Li, D. Bi, C. Yi, J. D. Décoppet, J. Luo, S. M. Zakeeruddin, A. Hagfeldt, M. Gratzel, *A vacuum flash-assisted solution process for high-efficiency large-area perovskite solar cells*, Science, 353, 6294, 2016.

[80] J. You, Y. Yang, Z. Hong, T.-B. Song, L. Meng, Y. Liu, C. Jiang, H. Zhou, W.-H. Chang, G. Li, Y. Yang, *Moisture assisted perovskite film growth for high performance solar cells*, Appl. Phys. Lett., 105, 183902, 2014.

[81] H. J. Queisser, E. E. Haller, *Defects in semiconductors: some fatal, some vital*, Science 281, 945-950, 1998.

[82] P. G. Le Comber, W. E. Spear, *Electronic transport in amorphous silicon films*, Phys. Rev. Lett., 25, 509-511, 1970.

[83] J. Nelson, *The Physics of Solar Cells*, Imperial College Press, 2003.

[84] H. Yu, X. Liu, Y. Xia, Q. Dong, K. Zhang, Z. Wang, Y. Zhou, B. Song, Y. Li, *Room-temperature mixed-solvent-vapor annealing for high performance perovskite solar cells*, J. Mater. Chem. A, 4, 321, 2016.

[85] D. Liu, L. Wu, C. Li, S. Ren, J. Zhang, W. Li, L. Feng, *Controlling $CH_3NH_3PbI_{3-x}Cl_x$ Film Morphology with Two-Step Annealing Method for Efficient Hybrid Perovskite Solar Cells*, ACS Appl. Mater. Interfaces, 7, 16330, 2015.

[86] J. L. Knutson, J. D. Martin, D. B. Mitzi, *TIning the band gap in hybrid tin iodide perovskite semiconductors using structural templating*, Inorganic Chemistry, 44(13), 4699-705, 2005.

[87] G. Grancini, S. Marras, M. Prato, C. Giannini, C. Quarti, F. De Angelis, M. De Bastiani, G. E. Eperon, H. J. Snaith, L. Manna, A. Petrozza, *The impact of the crystallization processes on the structural and optical properties of hybrid perovskite films for photovoltaics*, The Journal of Physical Chemistry Letters, 5 (21), 3836-3842, 2014.

[88] C. Quarti, G. Grancini, E. Mosconi, P. Bruno, J. M. Ball, M. M. Lee, H. J. Snaith, A. Petrozza, F. De Angelis, *The Raman spectrum of the CH3NH3PbI3 hybrid perovskite: interplay of theory and experiment*, The Journal of Physical Chemistry Letters, 5 (2), 279-284, 2013.

[89] G. Grancini, A. R. S. Kandada, J. M. Frost, A. J. Barker, M. De Bastiani, M. Gandini, S. Marras, G. Lanzani, A. Walsh, A. Petrozza, *Role of microstructure in the electron–hole interaction of hybrid lead halide perovskites*, Nature Photonics, 9 (10), 695-701, 2015.

[90] M. Saba, M. Cadelano, D. Marongiu, F. Chen, V. Sarritzu, N. Sestu, C. Figus, M. Aresti, R. Piras, A. G. Lehmann, C. Cannas, A. Musinu, F. Quochi, A. Mura, G. Bongiovanni, *Correlated electron-hole plasma in organometal perovskites*, Nature communications, 5, 2014.

[91] Q. Dong, Y. Fang, Y. Shao, P. Mulligan, J. Qiu, L. Cao, J. Huang, *Electron-hole diffusion lengths > 175 μm in solution-grown $CH_3NH_3PbI_3$ single crystals*, Science, 347, 6225, 2015.

[92] M. De Bastiani, G. Dell'Erba, M. Gandini, V. D'Innocenzo, S. Neutzner, A.R.S. Kandada, G. Grancini, M. Binda, M. Prato, J.M. Ball, M. Caironi, A. Petrozza, *Ion migration and the role of preconditioning cycles in the stabilization of the J-V characteristics of inverted hybrid perovskite solar cells*, **Advanced Energy Materials** 6 (2), 2016.

[93] L. Protesescu, S. Yakunin, M. I. Bodnarchuk, F. Krieg, R. Caputo, C. H. Hendon, R. X. Yang, A. Walsh, M. V. Kovalenko, *Nanocrystals of Cesium Lead Halide Perovskites ($CsPbX_3$, X = Cl, Br, and I): Novel Optoelectronic Materials Showing Bright Emission with Wide Color Gamut*, Nano Letters, 15, 3692 - 3696, 2015.

[94] F. Zhang, H. Zhong, C. Chen, X. Wu, X. Hu, H. Huang, J. Han, B. Zou, Y. Dong, *Brightly Luminescent and Color-Tunable Colloidal $CH_3NH_3PbX_3$ (X = Br, I, Cl) Quantum Dots: Potential Alternatives for Display Technology*, ACS Nano, 9 (4), 4533 - 4542, 2015.

[95] Y. S. Zhao, H. B. Fu, A. D. Peng, Y. Ma, D. B. Xiao, J. N. Yao, *Low-Dimensional Nanomaterials Based on Small Organic Molecules: Preparation and Optoelectronic Properties*, Adv. Mater., 20, 2859 - 2876, 2008.

[96] Y. W. Niu, F. Zhang, Z. L. Bai, Y. P. Dong, J. Yang, R. B. Liu, B. S. Zou, J. B. Li, H. Z. Zhong, *Aggregation-Induced Emission Features of Organometal Halide Perovskites and Their Fluorescence Probe Applications*, Adv. Opt. Mater., 3, 112 - 119, 2014.

[97] C. Bi, Q. Wang, Y. Shao, Y. Yuan, Z. Xiao, J. Huang, *Non-wetting surface-driven high-aspect-ratio crystalline grain growth for efficient hybrid perovskite solar cells*, Nat. Communications, 6, 2015.

[98] M. L. Petrus, Y. Hu, D. Moia, P. Calado, A. M. A. Leguy, P. R. F. Barnes, P. Docampo, *The Influence of Water Vapor on the Stability and Processing of Hybrid Perovskite Solar Cells Made from Non-Stoichiometric Precursor Mixtures*, ChemSusChem 9, 18, 2699 - 2707, 2016.

[99] G. Zorn, S. R. Dave, X. Gao, D. G. Castner, *Method for determining the elemental composition and distribution in semiconductor core-shell quantum dots*, Anal. Chem., 83, 866 - 873, 2011.

[100] J. Q. Grim, S. Christodoulou, F. Di Stasio, R. Krahne, R. Cingolani, L. Manna, I. Moreels, *Continuous-wave biexciton lasing at room temperature using solution-processed quantum wells*, Nature Nanotechnology, 9, 891–895, 2014.

[101] I. Moreels, G. Rainò, R. Gomes, Z. Hens, T. Stöferle, R. F. Mahrt, *Nearly temperature-independent threshold for amplified spontaneous emission in colloidal CdSe/CdS quantum dot-in-rods*, Adv. Mater., 24, 2012.

[102] E. Edri, S. Kirmayer, M. Kulbak, G. Hodes, and D. Cahen, *Chloride inclusion and hole transport material doping to improve methyl ammonium lead bromide perovskite-based high open-circuit voltage solar cells*, J. Phys. Chem. Lett. 5, 429-433, 2014.

[103] M. Kulbak, S. Gupta, N. Kedem, I. Levine, T. Bendikov, G. Hodes, D. Cahen, *Cesium enhances long-term stability of lead bromide perovskite-based solar cells*, J. Phys. Chem. Lett. 7, 2016.

[104] W. Nie, H. Tsai, R. Asadpour, J. C. Blancon, A. J. Neukirch, G. Gupta, J. J. Crochet, M. Chhowalla, S. Tretiak, M. A. Alam, H. L. Wang, A. D. Mohite, *High-efficiency solution-processed perovskite solar cells with millimeter-scale grains*, Science, 347, 6221 (522-5), 2015.

[105] R. J. Sutton, G. E. Eperon, L. Miranda, E. S. Parrott, B. A. Kamino, J. B. Patel, M. T. Hörantner, M. B. Johnston, A. A. Haghighirad, D. T. Moore, H. J. Snaith, *Band-gap-Tunable Cesium Lead Halide Perovskites with High Thermal Stability for Efficient Solar Cells*, Adv. Energy Materials, 6, 8, 2016.

[106] R. E. Beal, D. J. Slotcavage, T. Leijtens, A. R. Bowring, R. A. Belisle, W. H. Nguyen, G. F. Burkhard, E. T. Hoke, M. D. McGehee, *Cesium Lead Halide Perovskites with Improved Stability for Tandem Solar Cells*, J. Phys. Chem. Lett., 7, 5, 2016.

[107] N. Giesbrecht, J. Schlipf, L. Oesinghaus, A. Binek, T. Bein, P. Müller-Buschbaum, P. Docampo, *Synthesis of perfectly oriented and micrometer-sized MAPbBr3 perovskite crystals for thin-film photovoltaic applications*, ACS Energy Lett. 1, 150-154, 2016.

[108] N. Arora, S. Orlandi, M. I. Dar, S. Aghazada, G. Jacopin M. Cavazzini, E. Mosconi, P. Gratia, F. De Angelis, G. Pozzi, M. Graetzel, M. K. Nazeeruddin, *High open-circuit voltage: fabrication of formamidinium lead bromide perovskite solar cells using fluorene-dithiophene derivatives as hole-transporting materials*, ACS Energy Lett. 1, 107-112, 2016.

[109] A. Swarnkar, A. R. Marshall, E. M. Sanehira, B. D. Chernomordik, D. T. Moore, J. A. Christians, T. Chakrabarti, J. M. Luther, *Quantum dot–induced phase stabilization of a-CsPbI3 perovskite for high-efficiency photovoltaics*, Science, 354, 6308, 2016.

[110] C. Tao, S. Neutzner, L. Colella, S. Marras, A.R.S. Kandada, M. Gandini, M. De Bastiani, G. Pace, L. Manna, M. Caironi, C. Bertarelli, A. Petrozza, *17.6% stabilized efficiency in low-temperature processed planar perovskite solar cells*, **Energy & Environmental Science** 8 (8), 2365-2370, 2015.

[111] P. Scherrer, *Bestimmung der inneren Struktur und der Grösse von Kolloidteilchen mittels Röntgenstrahlen*, Gottingen. Mathematisch-Physikalische Klasse, 2, 1918.

[112] K. Dongyoon, H. Hyun, B. Kang-Jun, K. Juhwan, K. Sun-Woo, K. Dong-Yu, N. Yong-Young, *Simple Bar-Coating Process for Large-Area, High-Performance Organic Field-Effect Transistors and Ambipolar Complementary Integrated Circuits*, Adv. Materials, 25, 31, 2013.

[113] J. Ouyang, T.-F. Guo, Y. Yang, H. Higuchi, M. Yoshioka, T. Nagatsuka, *High-performance, flexible polymer light-emitting diodes fabricated by a continuous polymer coating process*, Adv. Materials, 14, 12, 2002.

List of publications

- V. D'Innocenzo, A. R. S. Kandada, M. De Bastiani, M. Gandini and A. Petrozza, *Tuning the light emission properties by band gap engineering in hybrid lead halide perovskite*, **Journal of the American Chemical Society** 136, 51, 2014.

- C. Tao, S. Neutzner, L. Colella, S. Marras, A.R.S. Kandada, M. Gandini, M. De Bastiani, G. Pace, L. Manna, M. Caironi, C. Bertarelli, A. Petrozza, *17.6% stabilized efficiency in low-temperature processed planar perovskite solar cells*, **Energy & Environmental Science** 8 (8), 2365-2370, 2015.

- G. Grancini, A.R.S.Kandada, J.M. Frost, A.J. Barker, M. De Bastiani, M. Gandini, S. Marras, G. Lanzani, A. Walsh, A.Petrozza, *Role of microstructure in the electron–hole interaction of hybrid lead halide perovskites*, **Nature Photonics** 9 (10), 695-701, 2015.

- M. De Bastiani, G. Dell'Erba, M. Gandini, V. D'Innocenzo, S. Neutzner, A.R.S. Kandada, G. Grancini, M. Binda, M. Prato, J.M. Ball, M. Caironi, A. Petrozza, *Ion migration and the role of preconditioning cycles in the stabilization of the J-V characteristics of inverted hybrid perovskite solar cells*, **Advanced Energy Materials** 6 (2), 2016.

- S.G. Motti, M. Gandini, A.J. Barker, J.M. Ball, A.R.S. Kandada, A. Petrozza, *Photoinduced Emissive Trap States in Lead Halide Perovskite Semiconductors*, **ACS Energy Letters** 1 (4), 726-730, 2016.

- A.R.S. Kandada, S. Neutzner, V. D'Innocenzo, F. Tassone, M. Gandini, Q.A. Akkerman, M. Prato, L. Manna, A. Petrozza, G. Lanzani, *Nonlinear Carrier Interactions in Lead Halide Perovskites and the Role of Defects*, **Journal of the American Chemical Society**, 138 (41), 13604-13611, 2016.

- M. Gandini and Q. A. Akkerman, F. Di Stasio, P. Rastogi, F. Palazon, G.Bertoni, J.M. Ball, M. Prato, A. Petrozza, L. Manna, *Strongly emissive perovskite nanocrystal inks for high-voltage solar cells*, **Nature Energy** 2, 16194, 2016.

◇ F. Lamberti, L. Litti, M. De Bastiani, R. Sorrentino, M. Gandini, M. Meneghetti, A. Petrozza, *High-Quality, Ligands-Free, Mixed-Halide Perovskite Nanocrystals Inks for Optoelectronic applications*, **Advanced Energy Materials** 7 (8), 2017.

◇ G. Grancini, D. Viola, M. Gandini, D. Altamura, E.A.A. Pogna, V. D'Innocenzo, I. Bargigia, C. Giannini, G. Cerullo, A. Petrozza, *Lattice Distortions Drive Electron–Hole Correlation within Micrometer-Size Lead-Iodide Perovskite Crystals*, **ACS Energy Letters** 2 (1), 265-269, 2017.

◇ A.J. Barker, A. Sadhanala, F. Deschler, M. Gandini, S.P. Senanayak, P.M. Pearce, E. Mosconi, A.J. Pearson, Y. Wu, A.R.S. Kandada, T. Leitjens, F. De Angelis, S.E. Dutton, A. Petrozza, R.H. Friend, *Defect-Assisted Photoinduced Halide Segregation in Mixed-Halide Perovskite Thin Films*, **ACS Energy Letters** 2 (6), 2017.

◇ G. Batignani, G. Fumero, A. R. S. Kandada, G. Cerullo, M. Gandini, C. Ferrante, A. Petrozza, T. Scopigno, *Probing Femtosecond Lattice Displacement upon Photo-carrier generation in Lead Halide Perovskite*, arXiv preprint, arXiv:1705.08687, paper now under revision.